Delft University of Technology

Alleviation of Propeller-slipstream-induced unsteady pylon loading by a flow-permeable leading edge

Sinnige, Tomas; Corte, Biagio Della; De Vries, Reynard; Avallone, Francesco; Merino-Martínez, Roberto; Ragni, Daniele; Eitelberg, Georg; Veldhuis, Leo L.M.

Important note
To cite this publication, please use the final published version (if applicable).
Please check the document version above.

Alleviation of Propeller-Slipstream-Induced Unsteady Pylon Loading by a Flow-Permeable Leading Edge

Tomas Sinnige,* Biagio Della Corte,† Reynard De Vries,‡ Francesco Avallone,§
Roberto Merino-Martínez,¶ Daniele Ragni,** Georg Eitelberg,†† and Leo L. M. Veldhuis††
Delft University of Technology, 2629 HS Delft, The Netherlands

The impingement of a propeller slipstream on a downstream surface causes unsteady loading, which may lead to vibrations responsible for structure-borne noise. A low-speed wind-tunnel experiment was performed to quantify the potential of a flow-permeable leading edge to alleviate the slipstream-induced unsteady loading. For this purpose, a tractor propeller was installed at the tip of a pylon featuring a replaceable leading-edge insert in the region of slipstream impingement. Tests were carried out with four flow-permeable inserts, with different hole diameters and cavity depths, and a baseline solid insert. Particle-image-velocimetry measurements showed that the flow through the permeable surface caused an increase in boundary-layer thickness on the pylon's suction side. This led to a local drag increase and reduced lift, especially for angles of attack above 6 deg. Furthermore, it amplified the viscous interaction with the propeller tip-vortex cores, reducing the velocity fluctuations near the pylon surface by up to 35%. Consequently, lower tonal noise emissions from the pylon were measured in the far field. This suggests that the desired reduction in surface pressure fluctuations was achieved by application of the flow-permeable leading edge.

Nomenclature

a	=	speed of sound, m/s
B	=	propeller blade count
BPF	=	blade-passage frequency; nB, Hz
b	=	pylon span, m
b_{insert}	=	pylon span affected by flow-permeable insert, m
C_L	=	lift coefficient; $L/q_\infty S$
C_p	=	pressure coefficient; $(p - p_\infty)/q_\infty$
C_T	=	propeller thrust coefficient; $T/\rho_\infty n^2 D^4$
c	=	pylon chord length, m
c_d	=	section drag coefficient; $d/q_\infty c$
c_l	=	section lift coefficient; $l/q_\infty c$
D	=	propeller diameter, m
D_a	=	effective diameter of microphone array, m
D_{hole}	=	hole diameter in flow-permeable surface, m
d	=	drag force per unit span, N/m
f	=	frequency, Hz
J	=	propeller advance ratio; V_∞/nD
L	=	lift force, N
l	=	lift force per unit span, N/m
N	=	number of image pairs used for averaging in particle-image-velocimetry measurements
n	=	propeller rotational speed, Hz
p	=	static pressure, Pa
p_∞	=	freestream static pressure, Pa
q_∞	=	freestream dynamic pressure, Pa
R	=	propeller radius, m
Re_c	=	Reynolds number based on pylon chord length
r	=	radial coordinate, m
S	=	pylon surface area, m²
SPL	=	sound-pressure level, dB
t_{cavity}	=	cavity depth underneath flow-permeable surface, m
$|V|$	=	in-plane velocity magnitude, m/s; $\sqrt{V_X^2 + V_Y^2}$
V_{disk}	=	effective velocity at the propeller disk estimated from one-dimensional actuator-disk theory, m/s
V_X, V_Y, V_Z	=	axial, lateral, and vertical velocity component, m/s
V_X', V_Y', V_Z'	=	fluctuation of axial, lateral, and vertical velocity component, m/s
V_∞	=	freestream velocity, m/s
X	=	axial coordinate from propeller center, m
X_{pyl}	=	axial coordinate from pylon leading edge, m
Y	=	lateral coordinate from propeller center, m; sideline distance, m
y_n	=	wall-normal coordinate, m
Z	=	vertical coordinate from propeller center, m; spanwise coordinate, m
α	=	angle of attack, deg
ΔC_D	=	relative drag increase due to application of flow-permeable insert PxxCy with respect to solid insert; $(C_{D_{\text{P}xx\text{C}y}} - C_{D_s})/C_{D_s}$
ΔR	=	microphone-array resolution, m
ΔSPL	=	sound-pressure-level reduction due to application of flow-permeable insert PxxCy with respect to solid insert; $SPL_s - SPL_{\text{P}xx\text{C}y}$, dB
$\Delta |V|$	=	change of in-plane velocity magnitude due to flow-permeable insert PxxCy with respect to solid insert; $|V|_{\text{P}xx\text{C}y} - |V|_s$, m/s
δ	=	boundary-layer thickness, m
ρ_∞	=	freestream air density, kg/m³
σ_p	=	permeability factor

*Ph.D. Candidate, Flight Performance and Propulsion Section, Faculty of Aerospace Engineering, Kluyverweg 1; T.Sinnige@tudelft.nl. Member AIAA.

†Ph.D. Candidate, Flight Performance and Propulsion Section, Faculty of Aerospace Engineering, Kluyverweg 1.

‡Ph.D. Candidate, Flight Performance and Propulsion Section, Faculty of Aerospace Engineering, Kluyverweg 1. Member AIAA.

§Assistant Professor, Aeroacoustics Section, Faculty of Aerospace Engineering, Kluyverweg 1; F.Avallone@tudelft.nl. Member AIAA.

¶Ph.D. Candidate, Aircraft Noise and Climate Effects Section, Faculty of Aerospace Engineering, Kluyverweg 1. Member AIAA.

**Assistant Professor, Aeroacoustics Section, Faculty of Aerospace Engineering, Kluyverweg 1. Member AIAA.

††Professor, Flight Performance and Propulsion Section, Faculty of Aerospace Engineering, Kluyverweg 1. Member AIAA.

$\sigma_{SPL}^{i \cdot BPF}$	=	standard deviation of measured sound pressure levels at ith blade-passage-frequency multiple, dB
σ_V	=	standard deviation of velocity component from particle image velocimetry, m/s
ϕ	=	blade angular position, deg
ϕ'	=	blade angular position relative to approximate position at impingement of tip vortex on pylon leading edge, deg
ω_Z	=	Z component of vorticity, 1/s
ω_Z^*	=	Z component of normalized vorticity; $\omega_Z D / V_{disk}$

Subscripts

insert	=	related to leading-edge insert
pres	=	pressure side
PxxCy	=	related to flow-permeable insert PxxCy
s	=	related to solid pylon
suc	=	suction side

Superscripts

insert	=	related to leading-edge insert
rms	=	root mean square
s	=	related to solid pylon

I. Introduction

PROPULSION systems employing advanced propellers can offer a significant reduction in fuel consumption as compared to turbofan engines [1], albeit at lower cruise velocity and potentially with higher noise levels. To minimize cabin noise and mitigate integration challenges, it is beneficial to position the propellers as far away as possible from the passenger seats in the cabin [2–5]. The propellers can be mounted in tractor or pusher configuration at the back of the fuselage via a separate support pylon, directly to the horizontal tailplane (as proposed previously by Goldsmith and Bowles [4] and Goldsmith [5]), or even to the wingtips. Because pusher propellers suffer from noise penalties due to wake-encounter phenomena [6–8], the tractor–propeller configuration is an attractive design option.

Tractor–propeller configurations feature two distinct interaction effects, which are similar for pylon-mounted, tailplane-mounted, and wingtip-mounted propellers. This paper considers the pylon-mounted configuration, as illustrated in Fig. 1. In such a case, the presence of the pylon perturbs the inflow to the propeller (upstream effect), whereas the impingement of the propeller slipstream on the pylon alters the pylon performance (downstream effect). The upstream disturbance of the propeller inflow caused by the pylon leads to nonuniform blade loading, introducing an additional noise source next to the steady loading and thickness noise generated by the isolated propeller [9]. The downstream effect (i.e., the periodic impingement of the propeller blade wakes and tip vortices on the pylon) results in time-varying loads with strong spanwise and chordwise gradients [10–12]. These unsteady pylon loads can excite structural vibrations, which are transmitted into the airframe and can be perceived by the passengers as structure-borne noise, thereby reducing passenger comfort [13]. For typical cruise flight conditions,

the upstream effect on the propeller loading is small [14], and the downstream effect is the dominant mechanism for the generation of harmonic loading [15].

The interior noise penalty due to the impingement of the propeller slipstream can be mitigated by either modifying the transmission path of the vibrations through the aircraft structure [16] or directly at the source by decreasing the amplitude of the unsteady aerodynamic loads. The latter could be achieved by using a pylon with a flow-permeable leading edge, which is also referred to as passive porosity. Such an approach has been studied numerically for unsteady stator loading due to the interaction between the rotor and stator in turbomachinery [17–19] and blade–vortex interaction noise for helicopter applications [20]. The work by Tinetti et al. [17–19] predicted reductions in unsteady loading of up to 21% by applying passive porosity at the leading edge of the stator. It was shown that mass flow going in and out of the porous medium changed the effective aerodynamic shape of the surface, thereby modifying the pressure distribution. In a similar way, treating the leading edge of a rotor blade with passive porosity reduced the amplitude of blade–vortex interaction noise by 30%, as shown by Lee [20]. More recently, a combined experimental–analytical study [21] discussed measurements of the potential of porous material for tonal source attenuation in rotor–stator interactions, with the experimental setup designed to match the reduced frequencies typical of rotor–rotor interactions for contrarotating open rotors. Tonal noise reductions of up to 5 dB were achieved for a stator vane with a NACA 0012 airfoil and perforated leading edge featuring a porosity distribution similar to that considered in the work of Tinetti et al. [17–19]. No measurements were taken of the impact of the perforated leading edge on the aerodynamic performance of the vane. Other research on porous materials has mostly focused on the mitigation of shock-wave/boundary-layer interactions [22], leading-edge noise in turbulent inflow [23], flap side-edge noise [24], and trailing-edge noise [25,26].

The results presented in Refs. [17–21] confirm that passive porosity alleviates the unsteady loads due to rotor–stator and blade–vortex interactions. However, so far, no work is available in the open literature that studies the potential of passive porosity to alleviate the unsteady loading caused by the impingement of a propeller slipstream on a downstream surface, for which wake-impingement and vortex-impingement phenomena occur simultaneously. The present paper reports a quantitative analysis of the time-averaged and unsteady performance of flow-permeable leading-edge inserts applied to alleviate unsteady pylon loading for tip-mounted tractor–propeller configurations. The design of the flow-permeable leading edges was based on the optimal configuration identified by Tinetti et al. [17–19] for rotor-wake impingement on stator vanes, without further optimization for the present application. The effects of the flow-permeable leading edges on the time-averaged and unsteady aerodynamic performance of the pylon were quantified by flowfield measurements, lift and drag evaluations, and far-field noise acquisitions. The resulting dataset provides unique experimental evidence of the potential of a flow-permeable leading edge to alleviate unsteady loading due to both wake impingement and tip-vortex impingement.

II. Experimental Setup

A. Wind-Tunnel Facility and Models

The experimental campaign was carried out in the low-turbulence tunnel at Delft University of Technology. This closed-loop wind tunnel features an octagonal test section of $1.80 \times 1.25 \times 2.60$ m, in which a maximal flow velocity can be reached of approximately 120 m/s. At the selected freestream velocity of 40 m/s, the turbulence level is below 0.1% (bandpass filtered between 2 and 5 kHz). An installed pylon-mounted tractor–propeller configuration was represented by positioning a pylon downstream of a propeller, as shown in Fig. 2. This setup is referred to as setup I in the remainder of the paper.

The four-bladed right-handed propeller with a diameter of 0.237 m was driven by a 5.5 kW three-phase induction motor. During all tests, the blade angle at 75% of the propeller radius ($r/R = 0.75$) was set to 23.9 deg. Additional details of the propeller geometry were provided
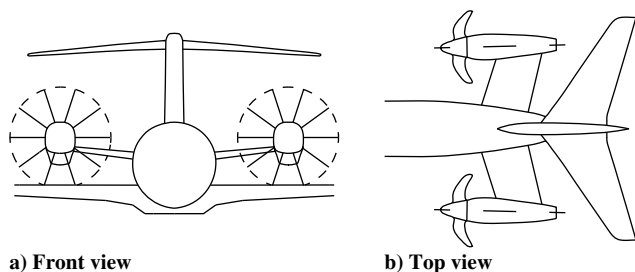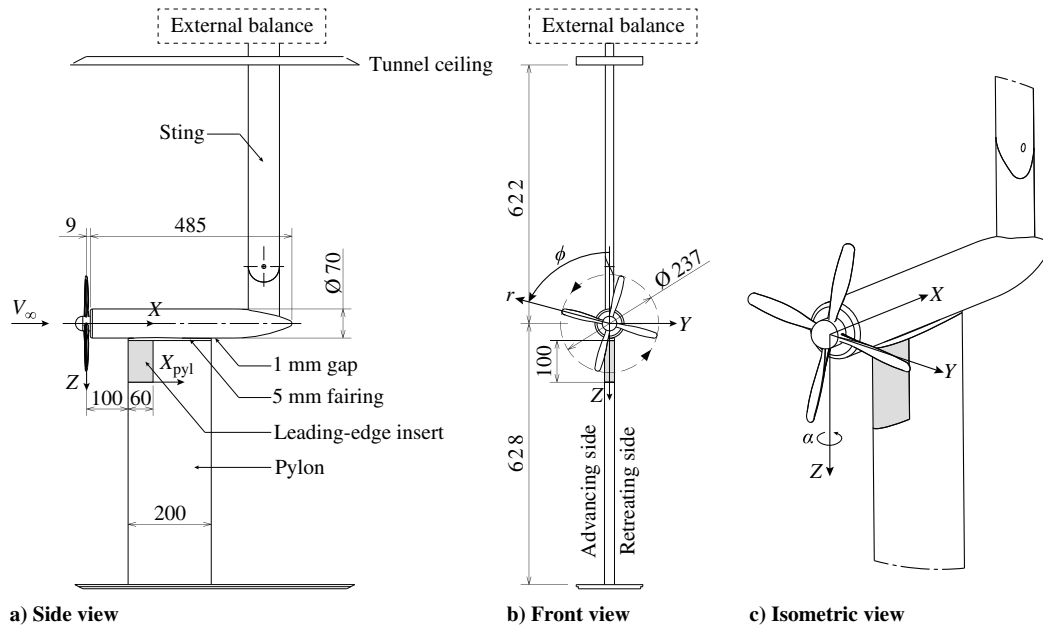

a) Front view   **b) Top view**
Fig. 1 Sketch of an aircraft layout with pylon-mounted tractor propellers. Based on Ref. [5].

a) Side view   **b) Front view**   **c) Isometric view**

Fig. 2   Experimental setup for the pylon–propeller interaction measurements (setup I). Dimensions in millimeters.
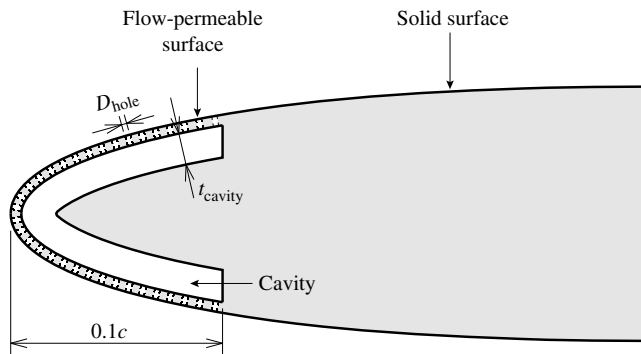

Fig. 3   Geometry of the flow-permeable leading-edge inserts.

in Ref. [12]. A support sting was used to connect the propeller to an external six-component balance. The pylon model featured a straight, untapered planform with a chord length of $c = 0.200$ m, a span of $b = 0.592$ m, and a NACA 0012 cross section. The leading edge of the pylon was positioned at 0.100 m from the propeller center, corresponding to an axial spacing of 0.42 times the propeller diameter.

A replaceable insert with a chord length of 0.060 m ($0.3c$) was integrated into the leading-edge region of the top part of the pylon, allowing for different treatments at the pylon leading edge. The span of the insert was 0.100 m, meaning that it extended up to 19% of the propeller radius below the tip of the propeller. A solid aluminum insert was used as a baseline configuration to which the performance of four different flow-permeable inserts was compared. The flow-permeable inserts were designed with a perforated skin covering an empty cavity underneath, as sketched in Fig. 3, and manufactured from polyamide by selective laser sintering. No optimizations were performed to define the characteristics of the flow-permeable inserts. Instead, the permeability distribution was taken from the work of Tinetti et al. [17–19] as the one that provided the best compromise between unsteady-load reductions and time-averaged airfoil performance for rotor–stator interactions. This meant a constant permeability of $\sigma_p^{max} = 0.22$ for $0 \leq X_{pyl}/c \leq 0.05$; after which, the permeability decreased elliptically down to $\sigma_p = 0.10$ over the range of $0.05 < X_{pyl}/c \leq 0.10$ [17–19]. The permeability factor σ_p is defined here as the ratio between open and closed surface areas. No barriers were placed in the cavity to allow for communication between the pressure and suction sides of the airfoil, again following the work of Tinetti et al. [17–19]. Different hole diameters D_{hole} and

cavity depths t_{cavity} were considered to study the sensitivity of the performance of the flow-permeable inserts to their design. Two hole diameters were used (equal to 0.5 and 1.0 mm, respectively) with a skin thickness of 1 mm. The default cavity depth was 3 mm, whereas for the model with holes of 0.5 mm, depths of 1 and 5 mm were also tested. An overview of the characteristics of the leading-edge inserts is provided in Table 1. The flow-permeable configurations are referred to as PxxCy, with xx as the hole diameter in millimeters multiplied by 10, and y as the cavity depth in millimeters. Figure 4 depicts a photograph of the P10C3 insert installed in the pylon downstream of the propeller.

Apart from modifying the unsteady loading, the installation of a flow-permeable leading edge also affects the time-averaged aerodynamic performance. This was quantified by measuring the lift and drag of an extended pylon model spanning the height of the test section (minus 2 mm gaps on both sides). The extended pylon featured the same profile and chord length as used for the pylon–propeller interaction measurements, whereas the replaceable inserts were positioned around the center of the wind tunnel. During these measurements, the propeller setup, including the nacelle and support sting, was removed. The resulting test setup is illustrated in Fig. 5, and it is referred to as setup II in the remainder of this paper. The results obtained with setup II cannot be compared directly to those acquired with the pylon–propeller setup (setup I; Fig. 2). Instead, they provide a general assessment of the time-averaged aerodynamic performance of the flow-permeable inserts, not accounting for specific installation details.

B.   Time-Averaged Pylon Loading Measurements Without Propeller

The impact of the flow-permeable leading edges on the lift and drag performance of the pylon was quantified using a wake rake, tunnel-wall pressure taps, and an external six-component balance. For these measurements, setup II was used (extended pylon; Fig. 5).

Table 1   Geometry characteristics of the leading-edge inserts

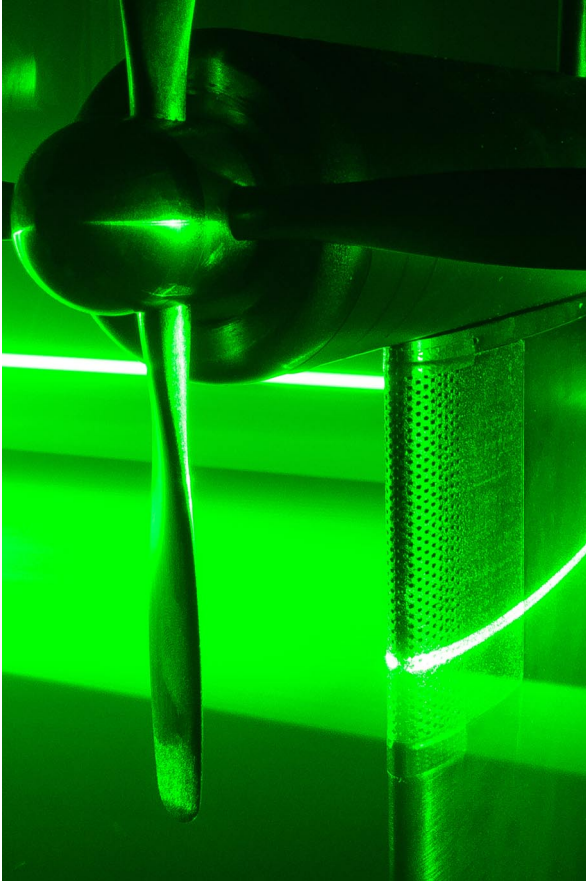| Configuration	D_{hole}, mm	t_{cavity}, mm
Solid	N/A[a]	N/A[a]
P05C1	0.5	1
P05C3	0.5	3
P05C5	0.5	5
P10C3	1.0	3

[a]N/A denotes "not applicable."

Fig. 4 P10C3 flow-permeable leading edge installed in pylon during particle-image-velocimetry measurements.

1. Pylon Lift

The lift generated by the pylon was measured with pressure taps distributed over four longitudinal strips installed in the walls of the test section. The pressure taps extended approximately $5c$ on both sides of the model along the tunnel walls. Therefore, a correction was required that accounts for the finite axial extent of the pressure taps. This was done following the method outlined in Ref. [27]. The pressure distribution associated with a point vortex at the model position was fitted to the measurement data to extrapolate the measured pressure distribution toward infinity in the up- and downstream directions. By integrating this pressure distribution and comparing the result to that obtained from integration of the original data, a lift correction factor is obtained. For the current test cases, this factor was equal to 1.13.

Because the flow-permeable inserts did not cover the entire span of the extended pylon model, the integrated lift obtained from the tunnel wall pressure data needed to be processed to obtain the performance of the flow-permeable part of the pylon. This was done by scaling the lift force with the spanwise extent of the pylon affected by the insert. This spanwise extent was determined from the measured wake-rake data (see Sec. II.B.2) as the vertical range over which the drag coefficient of the pylon with a flow-permeable insert was different from that obtained for the solid pylon; see Fig. 6. The lift on the remainder of the pylon was considered the same for all configurations:

$$C_L = c_l^s \left(\frac{b - b_{\text{insert}}}{b} \right) + c_l^{\text{insert}} \frac{b_{\text{insert}}}{b} \tag{1}$$

where b is the span of the extended pylon model (Fig. 5), b_{insert} is the spanwise extent of the pylon affected by the flow-permeable insert (Fig. 6), C_L is the lift coefficient of the entire pylon (measured), c_l^{insert} is the section lift coefficient of the flow-permeable insert (unknown), and c_l^s is the section lift coefficient of the solid pylon (known from measurements with the solid pylon).

2. Pylon Drag

The sectional drag of the pylon was measured with a wake rake positioned at $2.6c$ downstream of the pylon trailing edge. At this position, the static pressure was verified to be recovered to the freestream value. The width of the rake equaled 0.504 m, over which 67 total-pressure probes and 16 static-pressure probes were distributed in two separate rows, which were offset in the vertical direction. The total-pressure probes were spaced non-equidistantly to
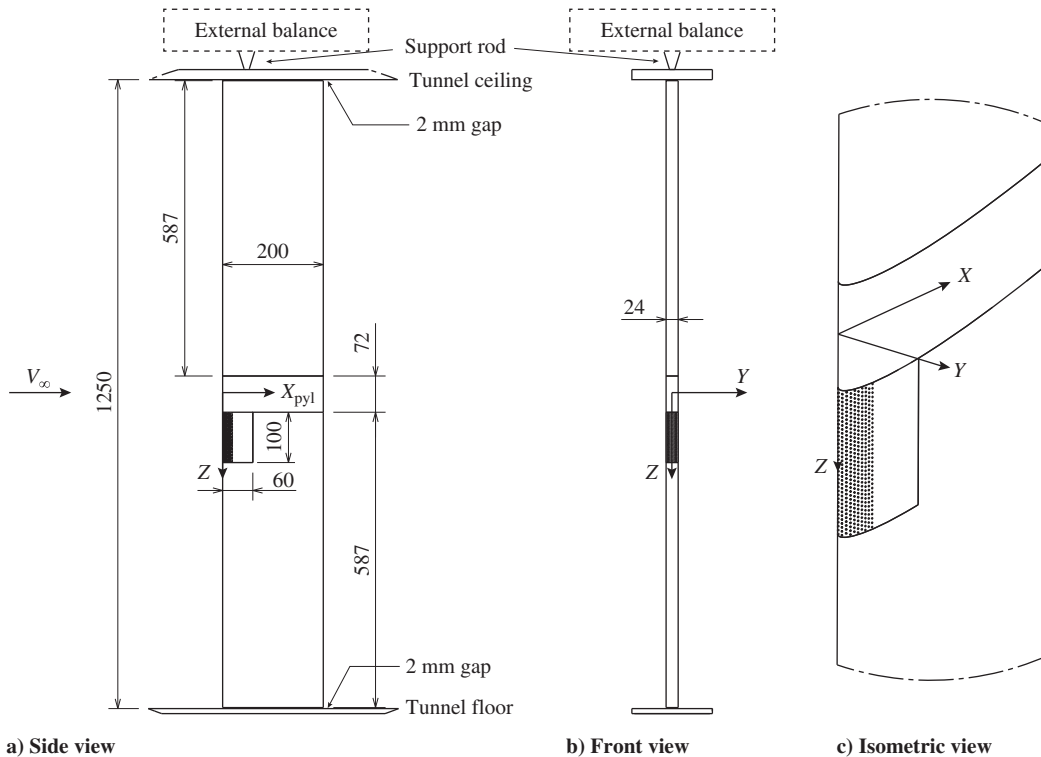

a) Side view   **b) Front view**   **c) Isometric view**

Fig. 5   Experimental setup for the pylon aerodynamic-performance measurements without propeller (setup II). Dimensions in millimeters.
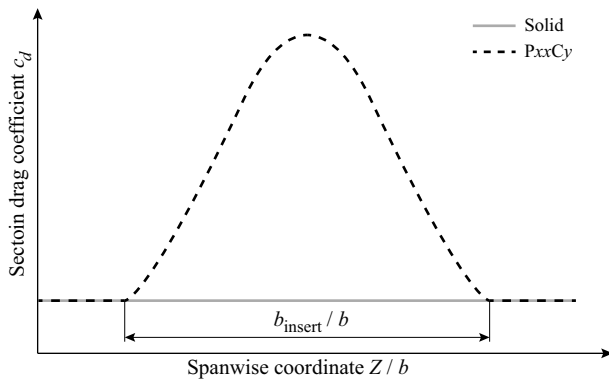
Fig. 6 Determination of spanwise extent of the pylon affected by the flow-permeable insert, based on typical measurement data for the sectional drag.

achieve a maximum resolution of 3 mm in the center part of the rake. The lateral position of the rake was changed for each data point to achieve this maximum spatial resolution over the entire pylon wake. All pressures were acquired simultaneously using an electronic pressure scanner recording at a sampling rate of 5 Hz. The wake rake was traversed in the vertical direction to acquire the sectional drag distribution in the wake of the pylon over a range of 1.5 times the chord length (0.300 m). Starting at $Z = c$, the wake rake was moved upward at a constant velocity of 2.5 mm/s while the pressure data were acquired.

As sketched in Fig. 6, the spanwise drag distributions for the configurations with flow-permeable leading-edge inserts showed a maximum near the center of the insert. The drag coefficient decreased toward the edges of the insert, eventually reaching the value obtained for the solid pylon. This was because only part of the pylon span was covered by the leading-edge insert. The maximum value measured over the span of the insert was taken here as a representative section drag coefficient of the insert. In this way, effects related to the finite span of the flow-permeable inserts were minimized. Consequently, the resulting performance figures are indicative of the sectional performance of an infinite-span pylon with a flow-permeable leading edge, and they do not account for typical three-dimensional effects encountered in installed configurations. Therefore, the presented section drag coefficients will be conservative as compared to those associated with actual installed flow-permeable inserts.

C. Particle-Image-Velocimetry Measurements

Particle-image-velocimetry (PIV) measurements were taken to map the flowfields in the slipstream-impingement region at the leading edge of the pylon (leading-edge field-of-view (LEFOV) setup) and surrounding the entire pylon chord (chordwise field-of-view (CWFOV) setup). The velocity data obtained with the LEFOV setup were processed to compute the associated pressure fields. Figure 7 displays a sketch of the measurement-plane locations with

respect to the model, whereas the acquisition and postprocessing characteristics of both setups are summarized in Table 2. Post-processing was performed with an iterative multigrid method [28], whereas the uncertainty of the instantaneous velocity components was quantified using the method by Wieneke [29]. Given the finite number of image pairs, the mean flowfields obtained from the measurements represent an estimate of the true mean of the velocity fields, with an associated nonzero statistical uncertainty (even if the uncertainty of the instantaneous velocity fields were zero). This uncertainty of the mean flowfields was computed based on the velocity variations between the uncorrelated samples and the number of samples used for averaging at each vector location ($\sigma_V/\sqrt{N}$). The uncertainty values listed in Table 2 are equal to the average uncertainty over the entire field of view. The uncertainty of the velocity components in the vortex core was up to 10 times larger. Note that, besides the contribution due to uncertainty of the instantaneous velocity fields, the statistical uncertainty of the mean also contains a contribution due to turbulence.

1. Propeller-Slipstream Impingement at the Pylon Leading Edge (LEFOV)

The effects of wake impingement and tip-vortex impingement on the flowfield near the pylon leading edge were quantified using the planar PIV setup referred to as LEFOV (Fig. 7a). The fields of view surrounded the leading-edge region of the pylon, extending up to approximately $X_{pyl}/c = 0.20$. Two cameras were used to synchronously capture the flowfield on each side of the pylon. The resulting vector fields were then combined in postprocessing. Illumination was provided by two lasers, with one on each side of the test section. Cameras and lasers were traversed simultaneously to obtain measurements at three vertical positions, which were characteristic of the wake-impingement region ($Z/R = 0.74$) and the tip-vortex-impingement region ($Z/R = 0.97$ and $Z/R = 1.01$). The locations of the two planes in the tip-vortex-impingement region were chosen to match the spanwise positions of maximum pressure fluctuations on the retreating and advancing blade sides of the pylon, respectively [12]. Both uncorrelated and phase-locked acquisitions were performed. Phase locking was achieved using an optical one-per-revolution trigger signal installed in the electric motor driving the propeller. Six different phase angles were considered, corresponding to time instances before, during, and after impingement of the tip vortex on the leading edge of the pylon. The phase angle at the approximate time of impingement was defined as $\phi' = 0$ deg, whereas the remaining measurements were taken at -17.5, -2.5, 5, 27.5, and 52.5 deg.

The phase-uncorrelated velocity fields were used to compute the pressure field at $Z/R = 0.97$ by solving the Poisson equation for the pressure, obtained from the incompressible Navier–Stokes equations. An extensive review of this technique is provided in Ref. [30]. Three-point central schemes were applied to compute the in-plane spatial derivatives. The Poisson equation, including the viscous terms, was then solved by means of the second-order scheme developed by Ragni et al. [31]. Neumann boundary conditions were
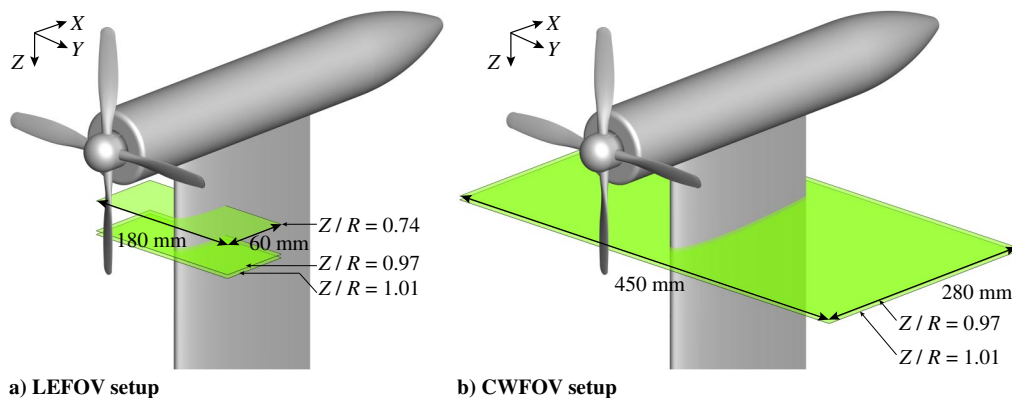

a) LEFOV setup   **b) CWFOV setup**

Fig. 7   Sketch of the measurement-plane locations for the PIV setups.

Table 2 Acquisition and postprocessing characteristics of the PIV setups

Parameter	LEFOV setup	CWFOV setup
PIV setup	Planar	Stereoscopic
Laser	2× Nd:YAG 200 mJ	1× Nd:YAG 200 mJ
Cameras	2 × 16 Mpixel	4 × 16 Mpixel
Imaging sensor	4872 × 3248 pixel, 7.4 × 7.4 μm/pixel, CCD[a] sensor	
Objective	200 mm $f/4$	200 mm $f/4$
Field-of-view size, mm	180 × 60	450 × 280
Field-of-view spanwise position	$Z/R = 0.74, 0.97, 1.01$	$Z/R = 0.97, 1.01$
Pulse separation, μs	5	19
Maximum particle displacement, pixel	10	12
Digital resolution, pixel/mm	50	12
Image pairs	300[b], 500[c]	250[b], 500[c]
Interrogation window size, pixels	24 × 24	48 × 48
Window overlap factor, %	50	50
Vector spacing, mm	0.2	2.0
Uncertainty instantaneous velocity magnitude	$0.018 V_\infty$	$0.039 V_\infty$
Uncertainty mean velocity magnitude	$0.002 V_\infty$[b], $0.003 V_\infty$[c]	$0.002 V_\infty$[b], $0.005 V_\infty$[c]

[a]CCD = charge-coupled device.
[b]Phase-locked measurements.
[c]Phase-uncorrelated measurements.

specified on the inflow and outflow boundaries and on the airfoil contour, whereas Dirichlet boundary conditions were used to prescribe the total pressure on the lateral sides of the domain, where the flow was isentropic. Because the LEFOV setup only allowed for planar PIV measurements, the out-of-plane velocity component was unavailable. However, previous work for similar configurations has shown that this component has a negligible impact on the results [31]. This was confirmed by an analysis of time-averaged pressure fields computed from the stereoscopic velocity data measured with the CWFOV setup.

The stochastic uncertainty of the pressure data was evaluated by propagating the statistical uncertainty of the PIV data through the routine used for the pressure computation. This was done by following a Monte Carlo approach, in which the pressure was computed repeatedly from the time-averaged velocity field with superimposed random noise. The noise was obtained from a normal distribution with zero mean and standard deviation equal to the 0.3% uncertainty of the mean (phase-uncorrelated) velocity data from PIV. A total of 10,000 iterations were performed, resulting in a converged standard deviation of the pressure coefficient of 0.04. Note that this error estimate does not include the propagation of a potential bias error in the PIV data.

2. Flowfield Around the Entire Pylon (CWFOV)

The stereoscopic CWFOV setup was employed to characterize the flowfield in a larger field of view surrounding the entire pylon (Fig. 7b). The CWFOV measurements were only taken for the solid and P10C3 configurations because the largest differences were expected to occur between these two cases. Four cameras were installed in two separate stereoscopic layouts, synchronously acquiring the flowfields on each side of the pylon. The resulting vector fields were then combined in postprocessing. A single laser was used to create light sheets on both sides of the pylon by splitting the laser beam, similar to the setup described in Ref. [32]. Only the tip-vortex-impingement region was considered, with measurement planes at $Z/R = 0.97$ and $Z/R = 1.01$. Phase-locked acquisitions were performed for a total of 17 phase angles to achieve high temporal resolution, whereas uncorrelated measurements were also taken.

D. Acoustic-Array Measurements

An acoustic array was used to measure the sound generated by the propeller and the leading-edge region of the pylon. The resulting far-field noise data served as indication of the source strength of the pressure fluctuations on the pylon surface. The array was integrated into the wall of the test section (retreating blade side) at a sideline distance of 0.9 m from the propeller center. Because the measurements were taken in the reverberant environment of a hard-walled test section, the array data may have been influenced by

acoustic reflections. However, the data were used to compare relative differences between configurations at the same frequency. In such a case, the effect of acoustic reflections is identical for all considered configurations, and thus will not affect the measured deltas.

The microphone array contained 64 PUI Audio POM-2735P-R microphones, with a sensitivity of -35 ± 2 dB (reference: 1 V/Pa) over a frequency range of 0.02–25 kHz. Each microphone was installed in a cavity covered by Kevlar fabric to reduce flow-induced noise stemming from the hydrodynamic pressure fluctuations in the boundary layer on the wind-tunnel wall. The microphone array had an approximately elliptical shape with a major axis in the flow direction of 0.93 m and a minor axis in the vertical direction of 0.48 m. Figure 8 displays the microphone locations with respect to the position of the models.

The microphone-array data were acquired at a sampling rate of 50 kHz and with a recording time of 120 s. The acoustic data were averaged with time blocks of 4096 samples for each Fourier transform and windowed using a Hann function with 50% data overlap. With these parameters, the frequency resolution was 12.2 Hz and the expected error of the cross-spectrum estimate [33] was 1.9%. Conventional frequency-domain beamforming [34] was applied to obtain the source maps, which were computed for a grid with 1 mm spacing. This grid was oriented parallel to the microphone array, intersecting with the propeller axis. The convection of sound waves was accounted for in the formulation of the steering vectors [35]. Furthermore, the main diagonal of the
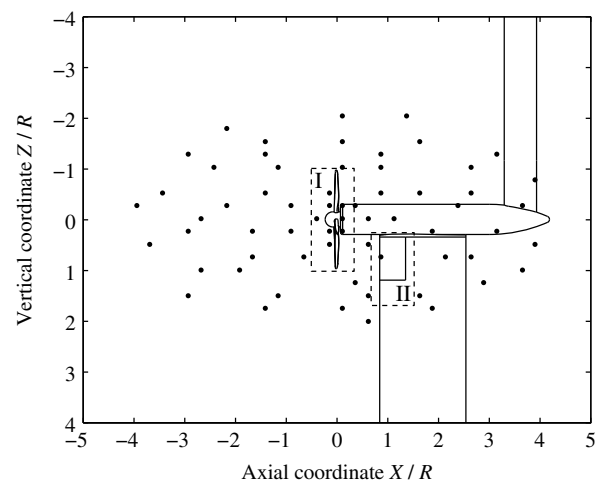

Fig. 8 Microphone locations with respect to the position of the models. Dashed boxes indicate the propeller (I) and pylon (II) integration sectors used for source power integration.

cross-spectral matrix was removed to suppress the effect of incoherent noise (mostly due to remaining pressure fluctuations caused by the boundary layer on the wind-tunnel wall) and improve the beamforming results [35].

The processed array data were used to synthesize the sound spectra emitted from the propeller and the leading-edge inserts by the technique of source power integration [35]. The two integration sectors used for this purpose are shown in Fig. 8. In each sector, the integrated beamforming results (per frequency) were normalized by the integral of a simulated unitary point source at the center of that integration sector, which was evaluated within the same spatial domain [36]. According to the Rayleigh criterion, the spatial resolution ΔR at the position of the scan plane ($Y = 0.9$ m) and at the blade-passage frequency ($f = BPF = 848$ Hz) equals approximately [35,37]

$$\Delta R = Y \tan\left(\frac{1.22a}{D_a f}\right) = 0.52 \text{ m} \qquad (2)$$

The effective diameter of the array D_a was taken here as the length of the array in the streamwise direction (0.93 m) because, in this case, the separation of sources in the flow direction is of interest, whereas the speed of sound a was considered at standard atmospheric conditions. The result of Eq. (2) implies that the sources due to the propeller and pylon could not be separated at the lowest frequencies because of the limited spatial resolution of the array. However, the array data could still be used to assess the relative change in the acoustic signature of the different pylon models with respect to the baseline solid configuration. This is discussed in more detail in Sec. III.C.3.

E. Description of Analyzed Test Cases

The measurements were taken at a freestream velocity of $V_\infty = 40$ m/s, corresponding to a Reynolds number based on the pylon chord length of approximately $Re_c = 550,000$. The major part of the test program was conducted under symmetric inflow conditions; hence, the angle of attack and angle of sideslip were equal to 0 deg. The two-dimensional aerodynamic performance of the pylon without the propeller, however, was also evaluated at nonzero incidence angles ranging from −6 up to +12 deg. A propeller operating condition was selected at which the blades were significantly loaded while preventing separated flow on the blade sections. At the selected blade pitch angle, this was achieved at a rotation frequency of 211.9 Hz, resulting in an advance ratio of $J = 0.8$. The corresponding thrust coefficient C_T equaled 0.095. The test results were not corrected for wind-tunnel wall effects.

III.   Results

A.   Time-Averaged Pylon Loading Without Propeller

The effect of the flow-permeable leading-edge inserts on the time-averaged aerodynamic performance of the pylon was initially considered without the propeller. The flowfield measurements were taken with setup I (pylon–propeller setup; Fig. 2) with the blades removed, whereas the performance data were acquired with setup II (extended pylon setup; Fig. 5).

1.   Flowfields Around the Leading-Edge Inserts

The LEFOV PIV setup (Sec. II.C.1) was used to characterize the flowfield around the leading-edge inserts at angles of attack of 0 and 6 deg. Figure 9 presents contours of the velocity magnitude measured around the solid leading-edge insert. These velocity fields served as a baseline to which the flowfields measured with the flow-permeable inserts were compared. Figure 10 provides contours of the resulting difference in velocity magnitude with respect to the solid pylon for the four flow-permeable configurations.

The velocity fields shown in Fig. 9 for the solid pylon display the expected features for a symmetric airfoil. At an angle of attack of 0 deg (Fig. 9a), the flowfield is symmetric, with a stagnation point at the leading edge of the profile. Increasing the angle of attack to 6 deg (Fig. 9b) causes the velocity to rise on the suction side of the pylon ($Y/c > 0$), whereas the stagnation point moves toward the pressure side of the airfoil.

The velocity-difference fields provided in Fig. 10 highlight the significant impact of the flow-permeable inserts on the flowfield, especially at a nonzero angle of attack. At an angle of attack of 0 deg (Fig. 10a), the velocity near the flow-permeable inserts increased around the stagnation point due to the local permeability of the pylon. Moreover, compared to the solid pylon, the boundary-layer thickness increased on both sides of the pylon. This is attributed to a combination of higher surface roughness, viscous losses in the holes and cavity of the flow-permeable inserts, and the change in effective outer shape due to flow passing through the flow-permeable inserts. Comparing the results for the different inserts, it can be concluded that the changes to the boundary-layer behavior become larger with increasing hole diameter and cavity depth.

When increasing the angle of attack to 6 deg (Fig. 10b), the pressure difference across the inserts increases. The effect of the P05C1 insert on the flowfield surrounding the pylon leading edge was relatively small. In contrast, a strong impact on the flowfield can be observed for the inserts with cavity depths of 3 and 5 mm. The thick boundary layer developing on the suction side of these inserts changed the effective thickness distribution of the airfoil, moving the suction peak downstream and decreasing its amplitude. The strong modification of the flowfield on this side of the pylon suggests that flow passed through the flow-permeable inserts from the pressure
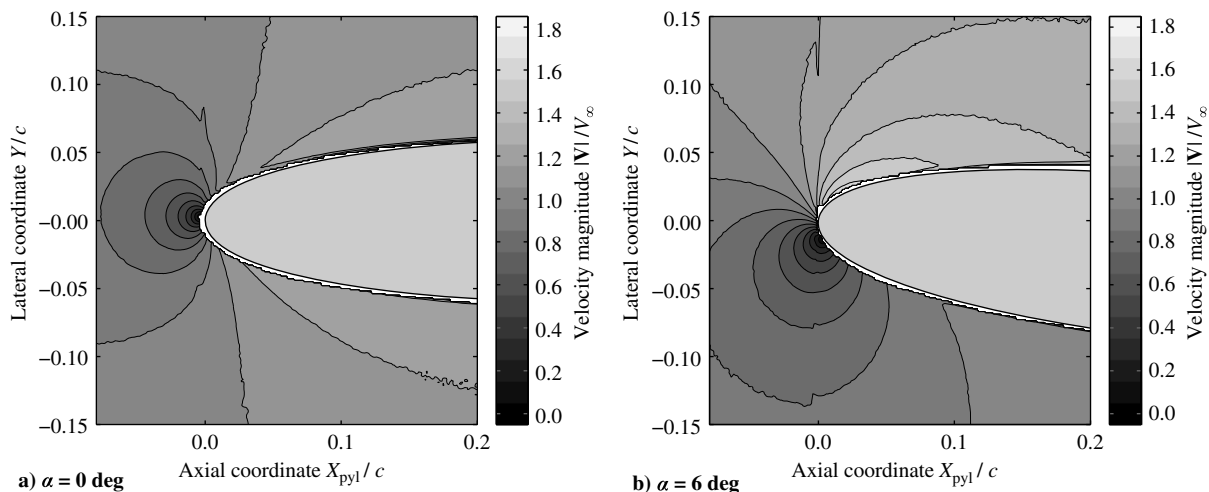

Fig. 9   Velocity magnitude around the solid leading-edge insert; propeller off, $Re_c = 550,000$.
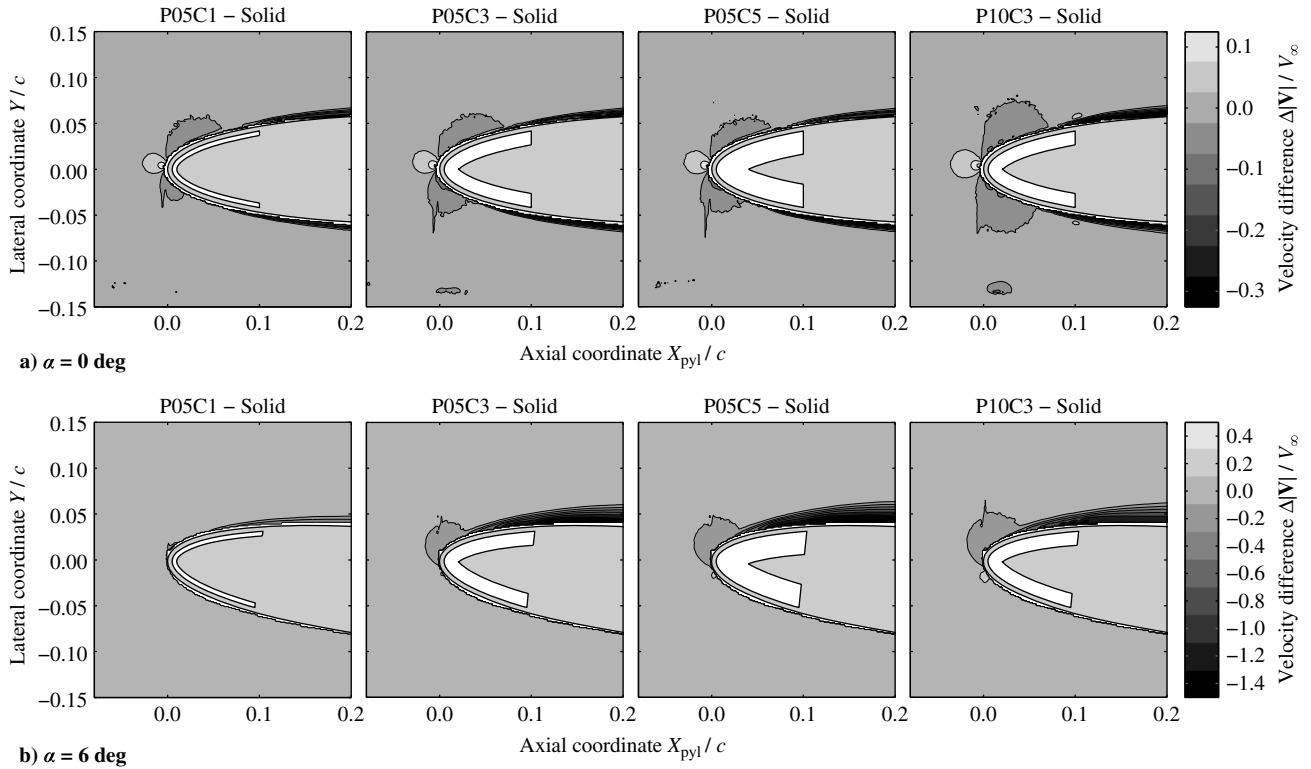
a) $\alpha = 0$ deg

b) $\alpha = 6$ deg

Fig. 10   Difference in velocity magnitude with respect to solid leading-edge insert; propeller off, $Re_c = 550{,}000$.

side to the suction side. To assess whether this throughflow was present, the lateral velocity component (in the Y direction) was analyzed near the suction side of the P10C3 insert. Figure 11 displays contours of both the time-averaged results and the rms of the instantaneous flowfields. The lateral velocity component is defined as positive in the positive Y direction; hence, outflow on this side of the insert would correspond to a positive lateral velocity.

The time-averaged data (Fig. 11a) show a pattern of narrow regions near the surface in which the amplitude of the lateral velocity was increased. The chordwise locations at which this occurred correspond to the chordwise locations of the holes in the P10C3 insert. This suggests that, indeed, flow passed through the holes of the

a) Mean velocity

b) Velocity fluctuations

Fig. 11   Lateral velocity component (Y direction) on the suction side of the P10C3 insert; $\alpha = 6$ deg, propeller off, $Re_c = 550{,}000$.

insert, which was then responsible for the changes to the flowfield displayed in Fig. 10. At the same locations, the fluctuations of the lateral velocity component (Fig. 11b) also peaked, with an rms level comparable to the magnitude of the time-averaged velocity. This could hint at a pulsating outflow from the flow-permeable insert, as discussed previously by Tinetti et al. [17,18]. Following the experimental work detailed in the present paper, a computational study was also performed with a similar geometry at the same operating conditions [38]. The numerical results obtained in that study support the outflow mechanism described in the present paper.

To quantify the changes to the boundary layer caused by the flow-permeable inserts, velocity profiles were extracted from the measured flowfields. Figure 12 presents the resulting velocity profiles on the suction side of the pylon as a function of the nondimensional wall-normal coordinate y_n/c. The corresponding boundary-layer profiles on the pressure side are shown in Fig. 13. Note that different ranges are used for the horizontal axis of both figures. Three chordwise positions are considered, corresponding to locations on top ($X_{pyl}/c = 0.08$), at the end ($X_{pyl}/c = 0.10$), and downstream ($X_{pyl}/c = 0.12$) of the flow-permeable part of the leading-edge inserts. Because of reflections, the boundary layers could not be resolved up to the surface of the pylon. Instead, the first data point is positioned at approximately $0.003c$ above the surface. The local boundary-layer thickness was approximated from the velocity profiles as the wall-normal coordinate of maximum velocity. Table 3 summarizes the data for both the suction side and the pressure side at $X_{pyl}/c = 0.12$, just downstream of the flow-permeable part of the inserts.

The boundary-layer profiles plotted in Figs. 12 and 13 confirm the conclusions drawn from the flowfields shown in Figs. 9–11. Compared to the solid pylon configuration, the cases with a flow-permeable leading-edge insert show a thickening of the boundary layer on the suction side. Moreover, the flow-permeable insert amplifies the growth of the boundary-layer thickness in the chordwise direction, as can be seen by comparison of Figs. 12a–12c. Both effects become stronger with increasing cavity depth, whereas the hole diameter has a smaller effect. On the pressure side, on the other hand, the boundary-layer thickness decreased for the P05C3, P05C5, and P10C3 configurations as compared to the solid baseline.
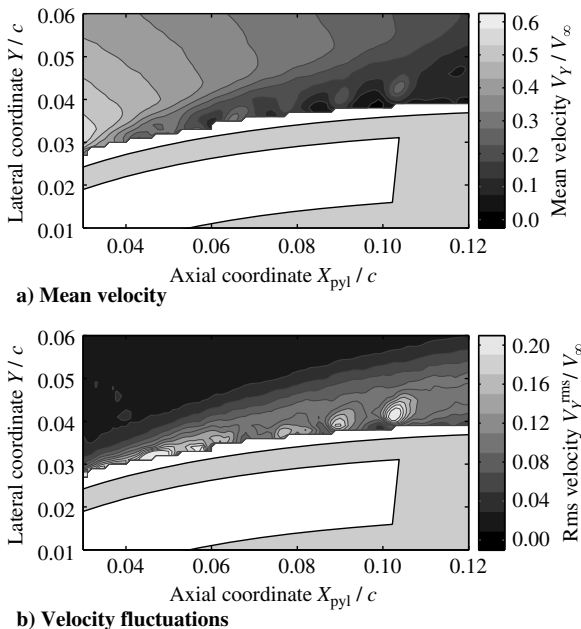
a) $X_{pyl}/c = 0.08$ b) $X_{pyl}/c = 0.10$ c) $X_{pyl}/c = 0.12$
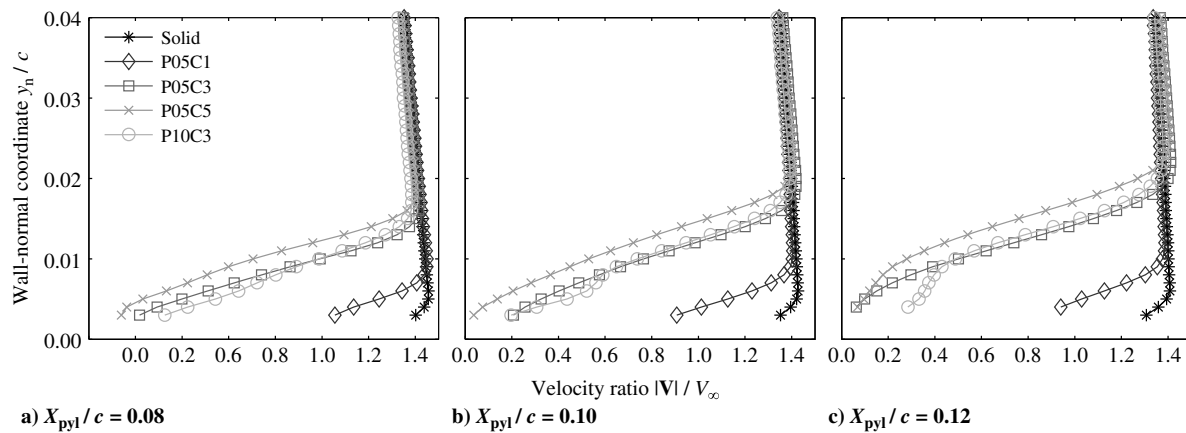
Fig. 12   Boundary-layer profiles on the suction side of the pylon; $\alpha = 6$ deg, propeller off, $Re_c = 550,000$.

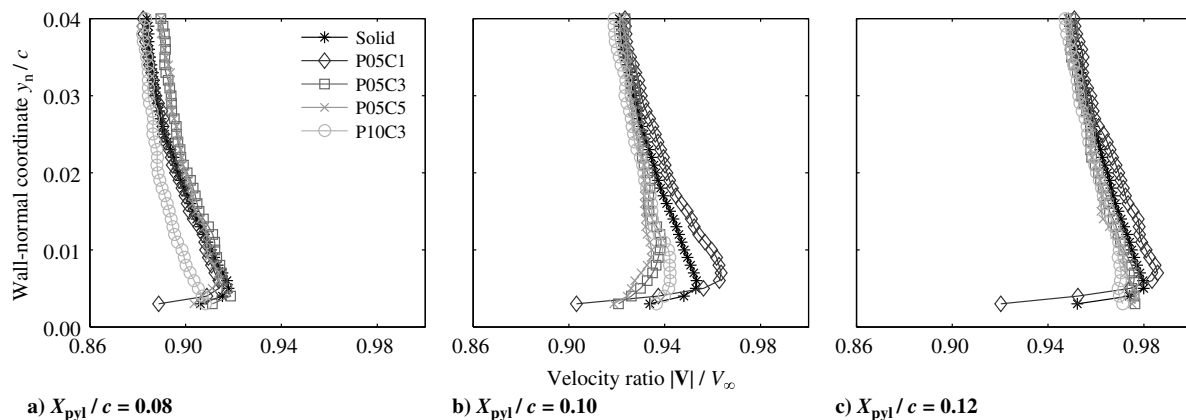a) $X_{pyl}/c = 0.08$ b) $X_{pyl}/c = 0.10$ c) $X_{pyl}/c = 0.12$

Fig. 13   Boundary-layer profiles on the pressure side of the pylon; $\alpha = 6$ deg, propeller off, $Re_c = 550,000$.

This is also shown by the data in Table 3, and it confirms that flow passed through the flow-permeable inserts from the pressure side to the suction side of the pylon. This is further supported by the departure in shape from a regular turbulent boundary layer that can be seen in Fig. 12 for the flow-permeable configurations. For the P10C3 insert, a change in slope of the velocity profile occurred at a wall-normal coordinate of around $y_n/c = 0.008$ at $X_{pyl}/c = 0.10$ (Fig. 12b) and $X_{pyl}/c = 0.12$ (Fig. 12c). A local increase in velocity can be seen, which is attributed to the additional momentum coming through the distinct holes in the leading-edge insert. The local velocity maxima could not be identified in the boundary-layer profiles for the configurations with the smaller hole diameter ($D_{hole} = 0.5$ mm). For these inserts, the throughflow is divided over a larger number of holes; hence, the viscous losses are higher and the local velocity perturbation through each hole is smaller than for the P10C3 insert.

2. Lift and Drag Performance

The changes to the flowfield caused by the flow-permeable insert affect the time-averaged lift and drag performance. This was quantified by measurements with setup II (extended pylon; Fig. 5).

Table 3   Effect of flow-permeable leading edges on the normalized boundary-layer thickness; $\alpha = 6$ deg, $X_{pyl}/c = 0.12$, propeller off, and $Re_c = 550,000$

Configuration	$(\delta/c)_{suc}$	$(\delta/c)_{pres}$
Solid	0.006	0.005
P05C1	0.012	0.007
P05C3	0.022	<0.003
P05C5	0.025	0.004
P10C3	0.023	<0.003

These measurements served as indication of the time-averaged effects of the flow-permeable inserts on the sectional lift and drag performance.

The average sectional lift performance of the leading-edge inserts was determined from the tunnel wall pressure-tap data following Eq. (1), as explained in Sec. II.B.1. The sectional drag was obtained from the wake-rake measurements, as discussed in Sec. II.B.2. Figure 14 presents the resulting sectional lift and drag as a function of angle of attack for the five pylon configurations. The lift data were obtained over an angle-of-attack range spanning from -6 up to $+12$ deg, whereas the drag measurements were taken at six angles of attack in the range of -6 up to $+9$ deg.

The lift polars depicted in Fig. 14a highlight the strong dependence of the lift performance at higher angles of attack on the design of the flow-permeable insert. For angles of attack between approximately -6 and $+6$ deg, the lift increased linearly with angle of attack for all inserts, with a lift gradient lower than the theoretical value of 2π expected from thin-airfoil theory. This was due to nonnegligible induced effects caused by the 2 mm gaps on both ends of the pylon (Fig. 5), which were implemented in the setup to allow for external balance measurements. Compared to the solid pylon, the configurations with the flow-permeable insert displayed a reduction of the lift slope. The performance decreased nonlinearly with increasing hole diameter and increasing cavity depth. Considering that the results for the P05C3 and P05C5 inserts were equivalent, it is concluded that increasing the cavity depth beyond a limit value no longer has a significant effect on the generated lift. The reduced performance of the flow-permeable inserts was due to the flow through the permeable surface, mitigating the pressure difference at the leading edge of the pylon. As shown in Figs. 9 and 10, the inflow and outflow mechanisms changed the effective outer shape of the insert. This resulted in a decrease in magnitude of the suction peak, and hence a reduction of the lift. Note that the PIV evaluations were

performed with setup I (propeller–pylon setup; Fig. 2), and thus the effective angle of attack at the measurement plane might have been different from the one experienced in the measurements taken with setup II (extended pylon; Fig. 5).

At higher angles of attack, the lift decreased significantly as compared to the solid baseline for the P05C3, P05C5, and P10C3 inserts. The strongest effect was observed for the insert with the largest hole diameter, for which the throughflow will have been the most severe. The insert with the smallest cavity depth (P05C1), on the other hand, displayed better performance. For this insert, the significant drop in lift at higher angles of attack only occurred at $\alpha = 12$ deg, whereas at lower angles of attack, the reduction in the section lift coefficient was within ± 0.05 as compared to the solid pylon.

Figure 14b displays increased drag due to installation of the flow-permeable inserts. This was as expected, considering the associated increase of the boundary-layer thickness shown in Sec. III.A.1. The insert with the smallest hole diameter and cavity depth (P05C1) displayed the smallest drag penalty. Compared to the solid insert, the development of drag coefficient with angle of attack was similar for this configuration, albeit at levels up to approximately two times higher. For the flow-permeable inserts with larger cavity depth, on the other hand, the drag coefficient started to increase rapidly at angles of attack of 6 deg and above. This matches with the flowfields presented in Figs. 9 and 10, as well as with the lift response observed in Fig. 14a.

3. Projected Lift Performance and Drag Penalty due to Flow-Permeable Inserts

The results provided in Fig. 14 show reduced lift and significantly increased drag for the flow-permeable inserts. However, the largest unsteady loading due to the slipstream interaction occurs at the spanwise location of tip-vortex impingement [12]. Therefore, in a realistic application, possibly only a small spanwise part of the pylon needs to be covered with porosity to achieve reductions of the unsteady loads. Consequently, the absolute lift and drag penalties for a pylon treated with a flow-permeable insert would be smaller than the change measured over the spanwise extent of the insert. Therefore, a projection was made of the aerodynamic performance of

a realistic pylon with flow-permeable treatment along 10% of the pylon span, hence only covering the spanwise part around the tip-vortex-impingement location. The corresponding effective aerodynamic span of the flow-permeable inserts was scaled based on the approach described in the discussion of Eq. (1). To approximately account for three-dimensional effects, this computation was performed based on the mean drag coefficient measured over the inserts, as opposed to taking the maximum value as done in Fig. 14. Figure 15a presents the resulting pylon lift as a function of angle of attack. In terms of the pylon drag, a drag penalty was computed relative to the results obtained for the solid baseline configuration, as shown in Fig. 15b.

Figure 15a highlights that application of a 10%-span flow-permeable leading edge hardly affects the lift performance of the pylon. This is particularly relevant for wing-mounted and tailplane-mounted configurations, for which the lifting performance of the aerodynamic surface is more important than for the pylon-mounted case. For the P05C1 configuration, only a slight reduction in lift can be observed at the highest angle of attack considered ($\alpha = 12$ deg). The other flow-permeable configurations would decrease the lift performance for angles of attack beyond 6 deg. The maximum drop in lift coefficient was approximately 15% at the highest angle of attack considered.

From Fig. 15b it can be seen that the projected drag increase for the complete pylon would be 5–100%, depending on the configuration and angle of attack. For the P05C1 configuration, the drag penalty remained within 10% at all studied angles of attack. The reduced drag penalty observed for this configuration at a nonzero angle of attack is due to boundary-layer transition on the solid baseline configuration. At a low angle of attack, the natural transition point on the solid pylon will have been more downstream than for the P05C1 configuration because of the lower surface roughness of the solid model. This corresponds to lower skin-friction drag for the solid pylon, and hence a drag penalty for the P05C1 configuration. At a higher angle of attack, on the other hand, the natural transition point on the solid pylon will have also moved toward the leading edge. As a result, the relative drag penalty of the P05C1 insert decreased at higher angles of attack. The P05C3, P05C5, and P10C3 inserts displayed larger drag
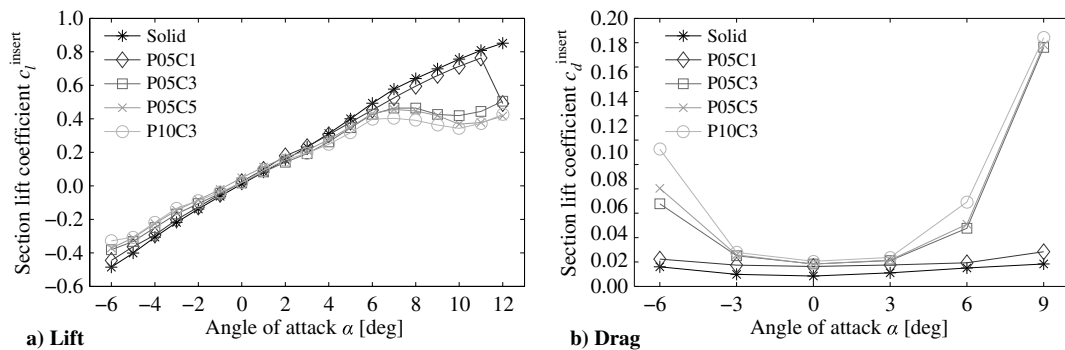

a) Lift   **b) Drag**

Fig. 14   Aerodynamic performance of the leading-edge inserts; $Re_c = 550{,}000$.

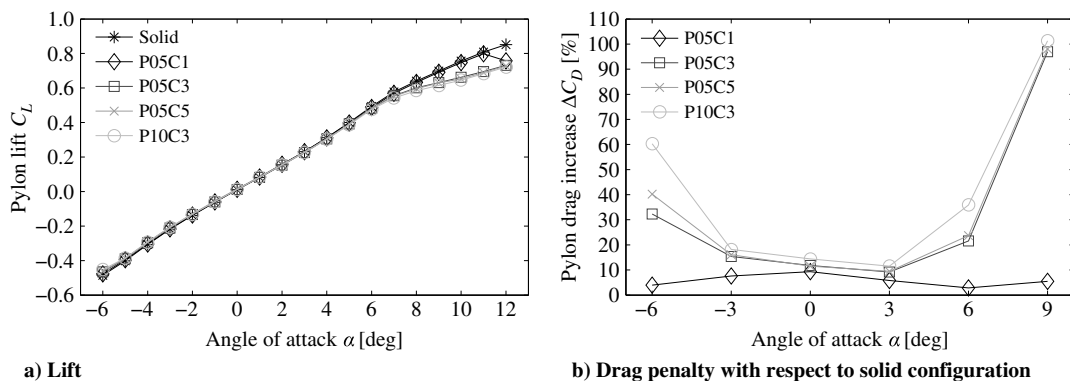**a) Lift**   **b) Drag penalty with respect to solid configuration**

Fig. 15   Projected aerodynamic performance for a pylon with 10% of the span treated with a flow-permeable leading edge; $Re_c = 550{,}000$.

penalties, especially at high angle of attack. This is as expected when considering the sectional drag performance of these inserts displayed in Fig. 14b. The largest increase in drag occurred for the P10C3 configuration, with a projected drag penalty of approximately 35% at an angle of attack of 6 deg.

At higher Reynolds numbers, which are more representative of flight, the extent of laminar flow on the solid pylon would decrease when compared to the situation in the experiment. The associated increased drag on the solid pylon would lead to a reduction of the relative drag penalty caused by the flow-permeable inserts, analogously to the preceding discussion of the impact of transition on the drag penalty of the P05C1 insert.

B. Time-Averaged Pylon Loading with Propeller

The time-averaged pylon loading with the propeller present was evaluated from the PIV measurements taken with the LEFOV setup (Sec. II.C.1). The computed pressure fields were used to extract pressure distributions as close as possible to the pylon, which corresponded to an offset of $0.0075c$ from the surface. Figure 16 presents the pressure distributions at vertical locations in the wake-impingement region ($Z/R = 0.74$, Fig. 16a) and tip-vortex-impingement region ($Z/R = 0.97$, Fig. 16b) for an angle of attack of $\alpha = 0$ deg. The pressure coefficient was defined based on the freestream dynamic pressure. The error bars shown in the top left of both subplots indicate the 95% confidence interval of the pressure data. Markers are displayed for clarity at chordwise intervals of $0.03c$; the actual resolution of the data was about 20 times higher (Table 2).

Compared to the solid pylon, the effect of the flow-permeable inserts on the pressure distribution was comparable in the wake-impingement region (Fig. 16a) and the tip-vortex-impingement region (Fig. 16b). For the flow-permeable configurations, the suction peak was displaced downstream toward the end of the flow-permeable part of the inserts and increased in magnitude as compared to the solid pylon. Similar modifications to the pressure distribution occur for a clean airfoil by increasing the profile thickness and/or moving the location of maximum thickness aft [27]. This matches with the change in the effective aerodynamic shape of the pylon observed before in Figs. 9 and 10 for the case without the propeller, which was attributed to crossflow through the flow-permeable inserts. Similar conclusions were drawn by Tinetti et al. [17–19] and Mineck and Hartwich [39]. The downstream displacement of the suction peak was also found in the numerical research of Lee [20]. In that case, however, the amplitude of the suction peak decreased due to the application of porosity. This can also be observed in the velocity fields of Fig. 10, but only at a higher effective angle of attack than for the data shown in Fig. 16.

For a given configuration, significant differences can be observed between the pressure distributions measured in the wake-impingement region ($Z/R = 0.74$; Fig. 16a) and the tip-vortex-impingement region ($Z/R = 0.97$; Fig. 16b). This is due to the radial gradients of the axial and tangential velocities in the propeller

slipstream. At $Z/R = 0.74$, the effect of the propeller is to increase the axial velocity. As a result, the local dynamic pressure is higher than the freestream dynamic pressure; hence, the pressure coefficient at the stagnation point increases beyond unity. Near the edge of the slipstream, on the other hand, the axial velocity increment is approximately zero; hence, the dynamic pressure is about equal to the freestream value. The distribution of the tangential velocity in the propeller slipstream causes an increased effective angle of attack at $Z/R = 0.74$. This leads to a stronger suction peak and larger pressure differential across the suction and pressure sides of the pylon than at the edge of the slipstream.

C. Unsteady Pylon Loading with Propeller

1. Flowfields Around the Leading-Edge Inserts

The time-dependent interaction between the propeller slipstream and the pylon leading edge was visualized using phase-locked PIV measurements with the LEFOV setup. Velocity data were acquired phase locked to the angular blade position for all five pylon configurations, as discussed in Sec. II.C.1. Figure 17 presents the corresponding velocity fields at time instants before, during, and after impingement of the tip vortex on the pylon leading edge. These time instants correspond to relative propeller blade phase angles of $\phi' = -17.5$ deg, $\phi' = 0$ deg, and $\phi' = +27.5$ deg, respectively, with $\phi' = 0$ deg taken as the phase angle corresponding to the blade location at the approximate time of tip-vortex impingement on the pylon leading edge. The measurements were taken at the tip-vortex-impingement location ($Z/R = 0.97$). An in-depth analysis of the tip-vortex-impingement process for the solid pylon configuration has been given by Sinnige et al. in Ref. [12]. The following discussion focuses on the changes to the flowfield induced by the flow-permeable leading edges.

Before impingement of the vortex on the pylon leading edge (Fig. 17a), the dominant effect of the flow-permeable inserts was to increase the boundary-layer thickness on the pylon, as discussed in Sec. III.A.1. The small angle of attack induced by the propeller slipstream changed the flowfields as compared to the propeller-off case shown in Figs. 9 and 10.

When the tip vortex impinges (Fig. 17b), it starts bending around the pylon leading edge. Initially, the flowfield remained practically unaffected by the application of the flow-permeable leading edge. However, once the vortex had traveled downstream (Fig. 17c), the effect of the flow-permeable inserts became more pronounced. The viscous interaction of the vortex with the pylon boundary layer leads to dissipation, reducing the strength of the vortex near the pylon surface [11]. This process is amplified when the boundary-layer thickness is increased. Moreover, the increased boundary-layer thickness also causes the vortex core to move away from the pylon surface, which is further enhanced by the outflow from the flow-permeable surface on the suction side of the model (Fig. 11).

Both the reduction in strength of the vortex and the displacement of the core away from the surface should reduce the pressure fluctuations on the pylon surface. In principle, these two effects could
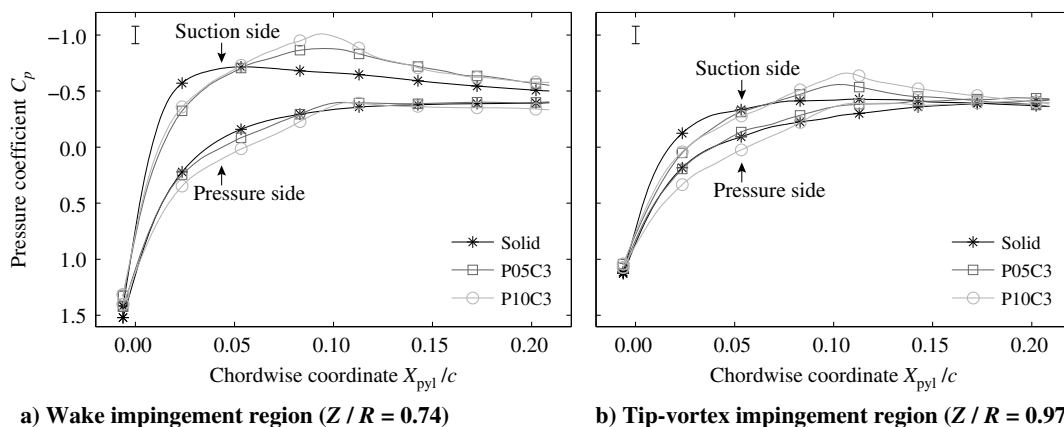

a) Wake impingement region ($Z/R = 0.74$)
b) Tip-vortex impingement region ($Z/R = 0.97$)
Fig. 16   Pressure distributions around the leading-edge inserts at $0.0075c$ from the surface; $\alpha = 0$ deg, $Re_c = 550,000$.
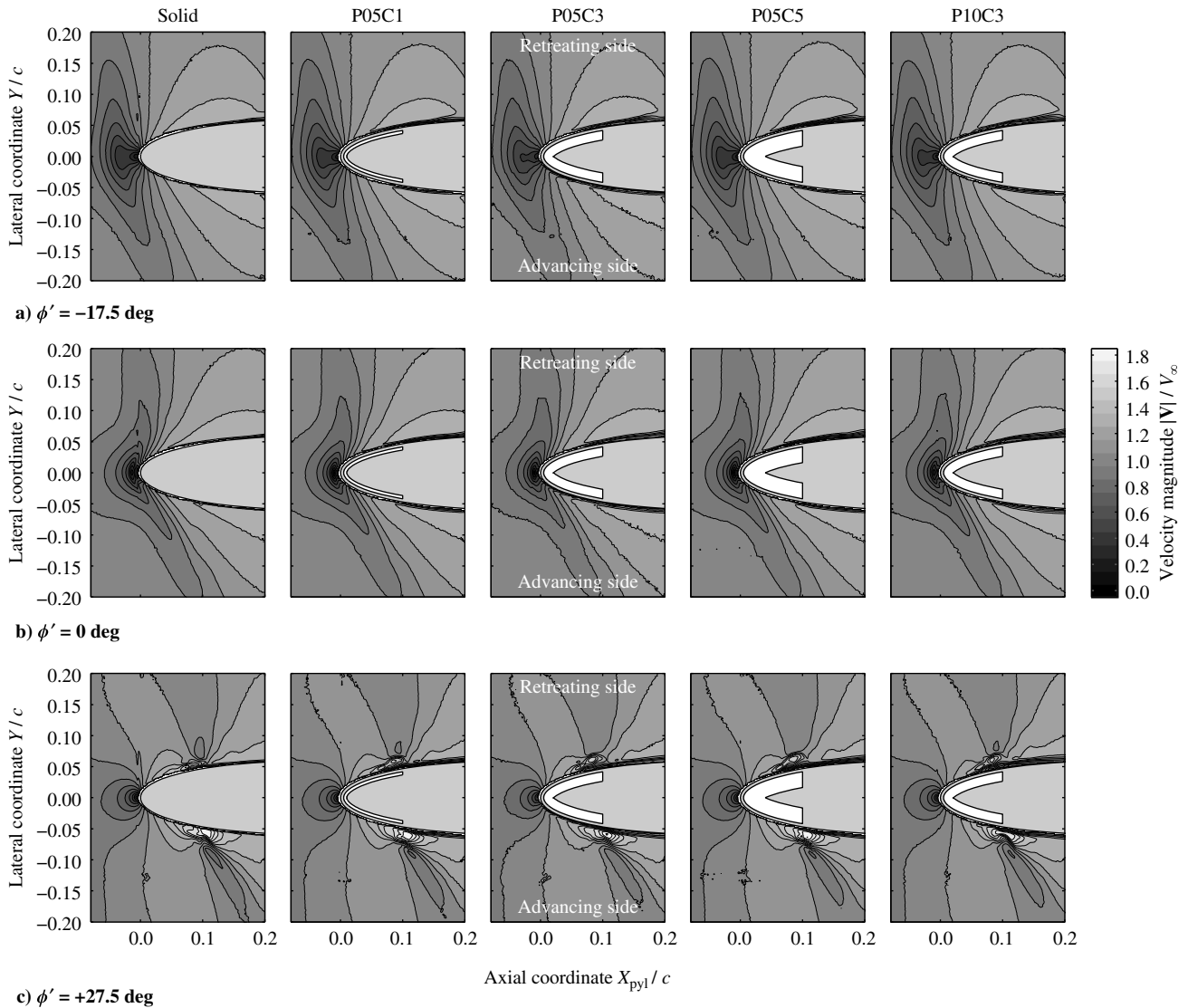
Fig. 17   Velocity fields before, during, and after impingement of the tip vortex on the pylon leading edge; $Z/R = 0.97$, $\alpha = 0$ deg, $Re_c = 550,000$.

also be achieved using a rough surface, assuming the same boundary-layer growth could be achieved as displayed here for the cases with a flow-permeable insert. However, the flow-permeable inserts enable two additional mechanisms: the flow through the holes and cavity leads to additional dissipation, whereas the communication between regions of high and low pressure alleviates local pressure gradients, and thus unsteady loading. These effects are smallest for the insert with the smallest cavity depth (P05C1), which is as expected when considering the flowfields measured for the propeller-off case (Figs. 9 and 10).

2. Flowfields Around the Entire Pylon

In addition to the local PIV measurements near the leading edge provided by the LEFOV setup, the CWFOV setup (Sec. II.C.2) was used to obtain phase-locked velocity fields around the pylon at the vertical position of tip-vortex impingement ($Z/R = 0.97$). For this setup, data are only available for the solid and P10C3 configurations. To illustrate the results obtained with the CWFOV setup, Fig. 18 presents an example phase-locked flowfield for the solid pylon configuration, displaying contours of the axial velocity. In addition to the velocity field, isolines of normalized vorticity $\omega_Z^* = \omega_Z D/V_{\text{disk}}$ are superimposed, where V_{disk} is the effective velocity at the propeller disk estimated from one-dimensional actuator-disk theory [40]. The two crosses in Fig. 18 indicate the positions at which velocity fluctuations were extracted, as presented in Fig. 19.

Figure 18 shows the tip vortices being convected downstream along the pylon chord. The expected spanwise shearing of the propeller slipstream [12] caused the vortex cores to gradually move away from the measurement plane on both sides of the pylon. On the advancing side, the vortices displace in the direction away from the propeller axis. As a result, the vortices crossed the measurement plane, as can be seen from the vorticity contours. This led to strong
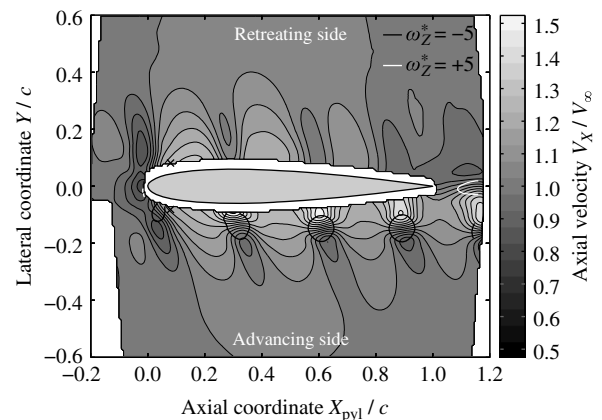

Fig. 18   Flowfield around the solid pylon; $Z/R = 0.97$, $\phi = 0$ deg, $\alpha = 0$ deg, $Re_c = 550,000$.

a) **Retreating side**
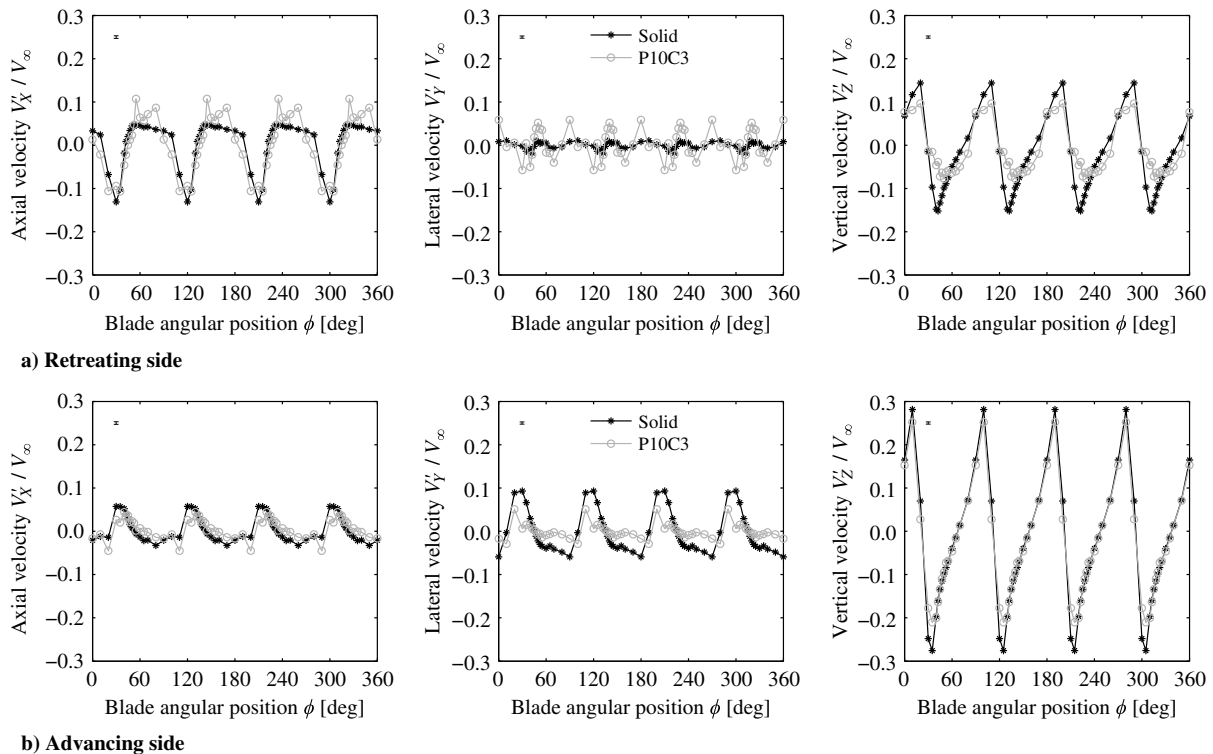

b) **Advancing side**

Fig. 19 Velocity fluctuations at $0.0375c$ from the pylon surface at $X_{pyl}/c = 0.08$ (i.e., at the markers indicated in Fig. 18); $Z/R = 0.97$, $\alpha = 0$ deg, $Re_c = 550{,}000$.

induced velocities in the field of view. On the retreating side, the slipstream edge displaces toward the propeller axis. Therefore, the vortices were above the measurement plane, and thus their effect on the measured velocity field was smaller.

To analyze the local unsteadiness near the pylon, time histories of the fluctuating velocity magnitude were extracted at $0.0375c$ from the surface at $X_{pyl}/c = 0.08$. Figure 19 presents the results for the solid and P10C3 configurations. The measurement data were acquired for a single blade passage only; these data were repeated for the remaining three blade passages to describe the response for a complete revolution. The error bar plotted in the top left of the subplots represents the 95% confidence interval of the respective velocity component from PIV.

The waveforms displayed in Fig. 19 highlight the strong effect of the tip-vortex passage on the velocity field around the pylon. Because locally the axis of the vortex was parallel to the Y axis and approximately in the measurement plane (see Ref. [12]), the tangential velocities induced by the vortex led to strong fluctuations of the vertical velocity component (in the Z direction). The rotation direction of the vortex was such that the vertical velocity increased (i.e., a velocity component away from the propeller axis) when the vortex approached the sampling location (see Fig. 2). The measured velocity fluctuations were largest on the advancing blade side, as expected from Fig. 18. This is due to the spanwise shearing of the slipstream, as discussed previously. Because of the tilting of the vortex path relative to the measurement plane, the induced velocities by the vortices also modified the other components of the velocity vector at the sampling location. The spanwise displacement away from the propeller axis on the advancing side led to an increase in axial velocity there, whereas the opposite occurred on the retreating side.

The flow through the holes and cavity of the flow-permeable insert at least partially mitigated the local velocity fluctuations caused by the periodic impingement of the tip vortices on the pylon. On the retreating side, the thicker boundary layer (Fig. 17) caused increased dissipation of the vortex as compared to the solid configuration, which is reflected by the reduced velocity fluctuations in the Z direction. Compared to the solid baseline, the rms level of the fluctuations decreased by about 35% by application of the

flow-permeable insert. The throughflow mechanism increased the fluctuations in the Y direction, albeit with small amplitude as compared to the other velocity components. On the advancing side, on the other hand, the velocity fluctuations in the Y direction decreased by the flow through the flow-permeable insert. This also seems to apply to the Z component; although, in that case, the peak amplitudes could be affected by the relatively coarse sampling. The reduced velocity fluctuations near the surface are promising in view of the desired reduction of the unsteady pylon loads.

3. Far-Field Acoustic Data

The flowfield information provided by the PIV measurements was complemented by far-field acoustic data acquired with the microphone array discussed in Sec. II.D. The impingement of the propeller slipstream on the pylon causes periodic velocity and pressure fluctuations on the pylon surface, as discussed in the previous sections. The pressure fluctuations lead to tonal noise radiated from the pylon. Although it will be shown that the sound pressure level of these tones is negligible as compared to the noise emitted by the propeller, the levels can still be used as an indirect measure of the unsteady pressure fluctuations on the pylon. Therefore, the potential mitigation of structure-borne noise offered by the flow-permeable inserts can be assessed by studying the far-field acoustic data measured with the microphone array.

Figure 20 presents example sound-source maps for the solid pylon at frequencies of two and five times the blade-passage frequency. The source maps confirm that the airborne noise associated with the pressure fluctuations on the pylon is negligible as compared to the steady-loading noise emitted by the propeller. However, the pressure fluctuations on the pylon may still be experienced as an additional noise source inside the cabin via the structure-borne noise path. Therefore, a reduction of these pressure fluctuations can increase passenger comfort.

To separate the sound emitted from the propeller and the pylon, source power integration was performed over the two sectors defined in Fig. 8. Figure 21 compares the resulting sound pressure levels for the different pylon configurations over a range of one-third-octave bands. It can be seen that the propeller noise was hardly affected by the pylon configuration, whereas the pylon noise decreased for two of
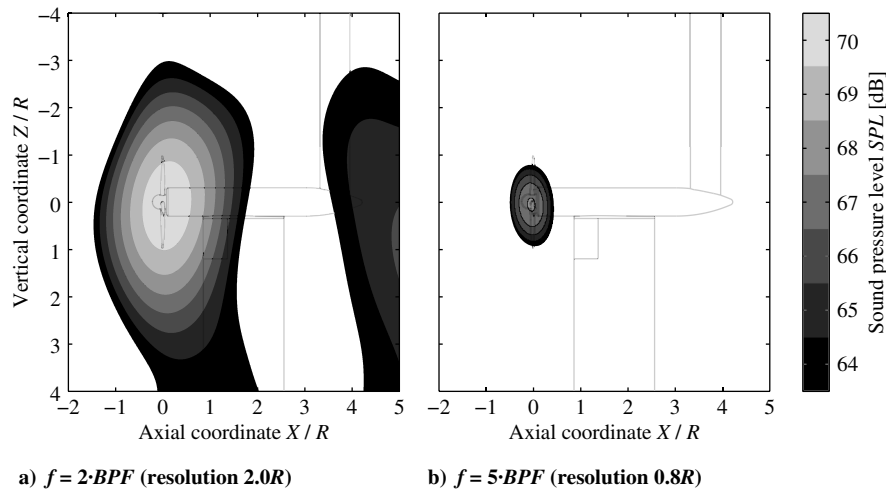
a) $f = 2 \cdot BPF$ (resolution 2.0R) b) $f = 5 \cdot BPF$ (resolution 0.8R)

Fig. 20 Sound-source maps for the solid pylon configuration; $Re_c = 550{,}000$.

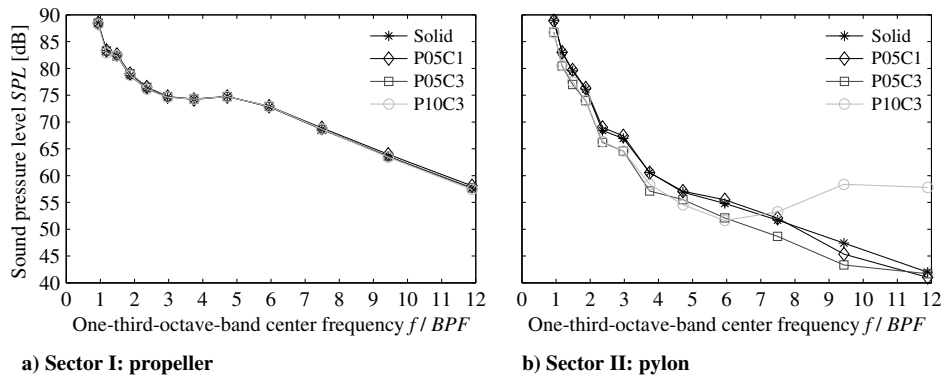a) Sector I: propeller b) Sector II: pylon

Fig. 21 One-third-octave-band sound pressure levels obtained from source power integration; $Re_c = 550{,}000$.

the flow-permeable inserts (P05C3 and P10C3) as compared to the solid baseline. Furthermore, a noise increase from the pylon can be observed at high frequency for the P10C3 configuration, albeit at levels significantly below the dominant noise at low frequency. These results are discussed in more detail in the following paragraphs.

At low frequency, the resolution of the microphone-array data was insufficient to distinguish the propeller and pylon noise sources [Eq. (2)]. As a result, the levels obtained in sector II (Fig. 21b) also contained a contribution due to the propeller. Although this effect gradually decreased with increasing frequency, it means that the data from sector II could only be used to study relative differences in sound emissions from the pylon with respect to the solid baseline configuration.

a. Propeller Noise. The upstream effect of the different leading-edge inserts on the propeller was investigated in more detail by analysis of the narrowband spectra of the propeller noise emissions, as determined by integration of the sound sources in the area surrounding the propeller (sector I in Fig. 8). Figure 22 presents the resulting spectra for a frequency range including the first four propeller tones. To illustrate the difference in upstream effect for the various pylon configurations, the standard deviation was computed from the tonal levels measured at each multiple of the blade-passage frequency. Small values of the resulting standard deviations indicate a limited upstream effect of the different inserts on the propeller noise.

Figure 22 shows that the propeller noise emissions were practically independent of the installed leading-edge insert. Propeller tones were recorded at the first four multiples of the blade-passage frequency, whereas broadband noise was dominant at higher frequencies. The variation in tonal levels for the different pylon configurations was lowest at the fundamental frequency ($f = 1 \cdot BPF$), for which the standard deviation of the measurements equaled 0.3 dB. The tonal amplitudes at the higher blade-passage-frequency multiples were
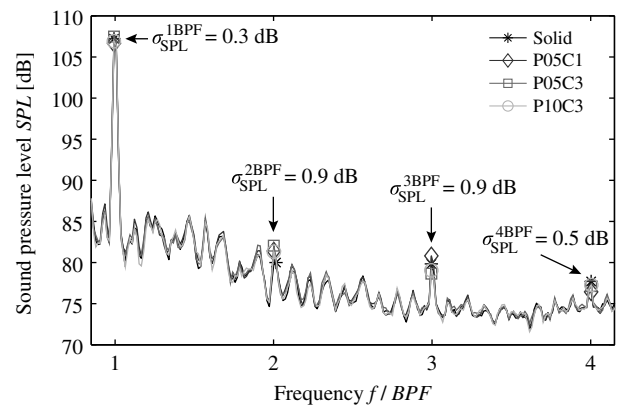

Fig. 22 Narrowband propeller noise spectra obtained from source power integration in sector I of Fig. 8; $Re_c = 550{,}000$.

lower, leading to an increased variation of at most ± 1 dB. When considering the one-third-octave-band levels (Fig. 21a), the standard deviation of the measurements for the different leading-edge inserts decreased to a maximum of 0.3 dB over the entire frequency range.

b. Pylon Noise. The small difference between the propeller noise spectra shown in Fig. 22 shows that the upstream effect of the pylon on the propeller did not depend on the installed leading-edge insert. Therefore, any difference between the measured noise signatures in the pylon integration area (sector II in Fig. 8) should have been due to a change in response at the pylon itself. Therefore, the far-field tonal noise extracted from the pylon sector could be used as an indirect measure of the pressure fluctuations on the leading-edge inserts.

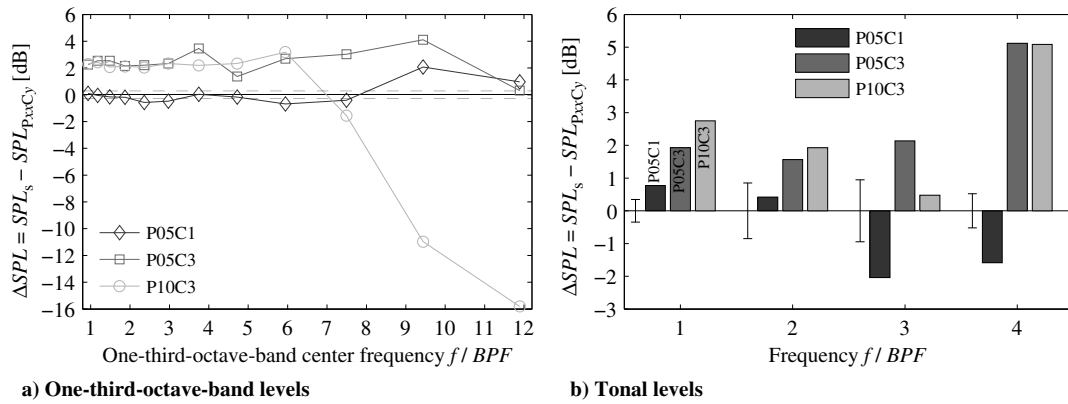a) One-third-octave-band levels b) Tonal levels

Fig. 23 Reduction in far-field acoustic pressure with respect to the solid pylon, obtained from source power integration in sector II of Fig. 8; $Re_c = 550,000$.
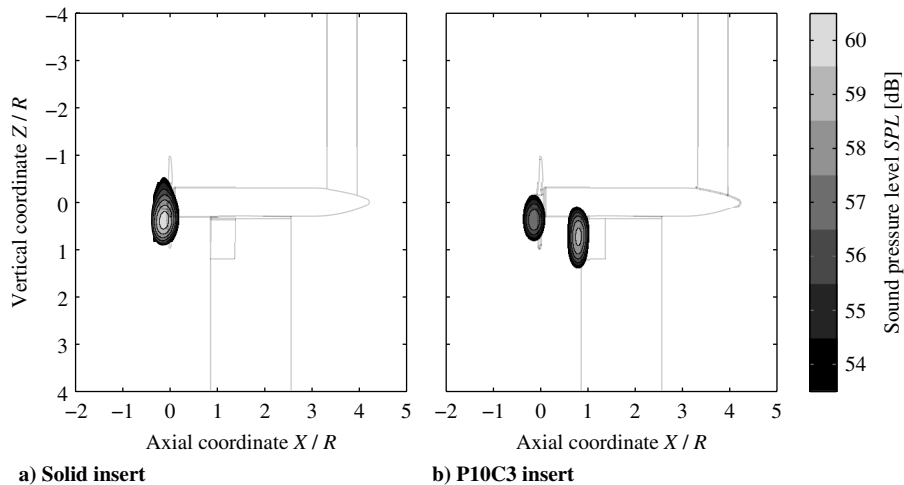

a) Solid insert b) P10C3 insert

Fig. 24 High-frequency broadband noise generation at the leading edge of the P10C3 insert; $6.7 \leq f/BPF \leq 13.4$ (resolution $< 0.6R$), $Re_c = 550,000$.

The results presented in Fig. 21b already indicated a change in noise emissions from the pylon for the different leading-edge configurations. Figure 23 presents the data as differences in sound pressure level with respect to the results recorded for the solid baseline configuration (ΔSPL). Positive values of ΔSPL indicate reductions of the measured sound pressure level by application of the flow-permeable inserts, and vice versa. Both the one-third-octave-band levels (Fig. 23a) and the tonal levels (Fig. 23b) are considered. The data uncertainty is indicated by the dashed lines in Fig. 23a and by the error bars in Fig. 23b. The associated values correspond to the standard deviation of the repeated propeller noise measurements (Fig. 22), evaluated as the maximum over each of the one-third-octave bands in Fig. 23a and separately at each multiple of the blade-passage frequency in Fig. 23b.

The one-third-octave-band data presented in Fig. 23a indicate that the P05C1 insert did not have a significant effect on the noise emissions from the pylon for frequencies up to about eight times the blade-passage frequency. The P05C3 and P10C3 inserts, on the other hand, provided a far-field noise reduction of 2 to 3 dB in this frequency range. This indicates that the pressure fluctuations on the surface were reduced by application of these flow-permeable inserts; hence, the interaction mechanism caused by the impingement of the propeller slipstream was at least partially mitigated. The observed differences between the P05C3 and P10C3 inserts were approximately within the measurement uncertainty for frequencies up to six times the blade-passage frequency.

At high frequency ($f/BPF > 7$), the P10C3 configuration displayed a strong noise increase as compared to the solid pylon. As shown in Fig. 24, the associated broadband noise source was found near the leading edge of the pylon and did not occur with the solid leading edge. The mechanism causing the noise penalty at higher

frequencies for the P10C3 insert is still unknown. However, it was also observed in numerical simulations of a similar geometry at the same operating conditions [38]. A previous study [26] focusing on porous treatments applied at the trailing edge of airfoils showed similar results, which were attributed to increased surface roughness due to the flow-permeable material. It should be noted that the absolute sound pressure level of the noise emissions in this frequency range was well below that at low frequency, and thus the additional noise-generating mechanism did not noticeably affect the overall sound pressure level.

The tonal levels shown in Fig. 23b confirm the observations made based on the one-third-octave-band levels. At the dominant fundamental frequency ($f = 1 \cdot BPF$), the P05C1 configuration returned a decrease in sound pressure level of only 0.8 dB, whereas the P05C3 and P10C3 configurations displayed reductions of 1.9 and 2.8 dB, respectively. For these two inserts, significant reductions of the far-field sound emissions also occurred for the higher harmonics. Therefore, it is concluded that the P05C3 and P10C3 inserts offered more effective unsteady-load alleviation than the P05C1 insert. This highlights the sensitivity of the unsteady-load alleviation to the cavity depth. Comparing the trends in unsteady-load alleviation with the time-averaged aerodynamic-performance data (Fig. 14), which indicated increased throughflow for the P05C3 and P10C3 inserts, it is concluded that the throughflow mechanism has a key impact on the unsteady-load alleviation obtained by the installation of the flow-permeable inserts.

IV. Conclusions

This paper has presented an experimental study focused on quantifying the potential of a flow-permeable leading edge to

alleviate the unsteady loading caused by propeller-slipstream impingement. A propeller was positioned upstream of a pylon featuring replaceable leading-edge inserts. A solid insert was used as a baseline to which the results obtained with four different flow-permeable inserts were compared.

From the velocity fields acquired with particle-image velocimetry, it is concluded that the application of a flow-permeable leading edge strongly modifies the flowfield around the pylon, especially at a nonzero angle of attack. The flow through the holes and cavity of the flow-permeable insert causes an increase in boundary-layer thickness, thereby modifying the effective outer shape of the pylon. This was particularly pronounced for the inserts with a larger cavity depth. The resulting lift performance was shown to be reduced, especially at angles of attack above 6 deg. Also, the drag increased, which was concluded to be the result of viscous dissipation and increased surface roughness as compared to the solid pylon model.

The increase in boundary-layer thickness resulted in a local reduction in strength of the propeller blades' tip vortices due to the enhanced viscous interaction, whereas the vortices also displaced away from the surface. Furthermore, the flow through the holes and cavity caused additional dissipation. Consequently, the velocity fluctuations induced by the blade tip vortices decreased by up to 35% near the pylon surface in the tip-vortex-impingement region. Microphone-array measurements showed that this led to reduced far-field noise, suggesting a reduction in pressure fluctuations on the pylon surface. Larger reductions in far-field noise, and thus pressure fluctuations, were obtained for the inserts with larger cavity depth. Because the time-averaged performance of the inserts decreased with increasing cavity depth, it is concluded that a careful tradeoff is required between time-averaged aerodynamic performance and unsteady-load alleviation when designing flow-permeable inserts.

References

[1] Guynn, M. D., Berton, J. J., Haller, W. J., Hendricks, E. S., and Tong, M. T., "Performance and Environmental Assessment of an Advanced Aircraft with Open Rotor Propulsion," NASA TM-2012-217772, Oct. 2012.

[2] Mann, S. A. E., and Stuart, C. A., "Advanced Propulsion Through the 1990s—An Airframer's View," *21st Joint Propulsion Conference*, AIAA Paper 1985-1192, July 1985.
doi:10.2514/6.1985-1192

[3] Page, M. A., Ivey, D. M., and Welge, H. R., "Ultra High Bypass Engine Applications to Commercial and Military Aircraft," *SAE Aerospace Technology Conference and Exposition*, SAE TP 861720, Long Beach, CA, Oct. 1986.
doi:10.4271/861720

[4] Goldsmith, I. M., and Bowles, J. V., "Potential Benefits for Propfan Technology on Derivatives of Future Short- to Medium-Range Transport Aircraft," *16th Joint Propulsion Conference*, AIAA Paper 1980-1090, June 1980.
doi:10.2514/6.1980-1090

[5] Goldsmith, I. M., "A Study to Define the Research and Technology Requirements for Advanced Turbo/Propfan Transport Aircraft," NASA CR-166138, Feb. 1981.

[6] Block, P. J. W., "Experimental Study of the Effects of Installation on Single- and Counter-Rotation Propeller Noise," NASA TP-2541, April 1986.

[7] Block, P. J. W., and Gentry, G. L., Jr., "Directivity and Trends of Noise Generated by a Propeller in a Wake," NASA TP-2609, Sept. 1986.

[8] Sinnige, T., Ragni, D., Malgoezar, A. M. N., Eitelberg, G., and Veldhuis, L. L. M., "APIAN-INF: An Aerodynamic and Aeroacoustic Investigation of Pylon-Interaction Effects for Pusher Propellers," *CEAS Aeronautical Journal*, Vol. 9, No. 2, 2018, pp. 291–306.
doi:10.1007/s13272-017-0247-2

[9] Magliozzi, B., Hanson, D. B., and Amiet, R. K., "Propeller and Propfan Noise," *Aeroacoustics of Flight Vehicles: Theory and Practice, Vol. 1: Noise Sources*, edited by H. H. Hubbard, NASA Langley Research Center, Hampton, VA, 1992, pp. 1–64.

[10] Ljunggren, S., Samuelsson, L., and Widing, K., "Slipstream-Induced Pressure Fluctuations on a Wing Panel," *Journal of Aircraft*, Vol. 26, No. 10, 1989, pp. 914–919.
doi:10.2514/3.45861

[11] Johnston, R. T., and Sullivan, J. P., "Unsteady Wing Surface Pressures in the Wake of a Propeller," *Journal of Aircraft*, Vol. 30, No. 5, 1993, pp. 644–651.
doi:10.2514/3.46393

[12] Sinnige, T., de Vries, R., Della Corte, B., Avallone, F., Ragni, D., Eitelberg, G., and Veldhuis, L. L. M., "Unsteady Pylon Loading Caused by Propeller-Slipstream Impingement for Tip-Mounted Propellers," *Journal of Aircraft*, Vol. 55, No. 4, 2018, pp. 1605–1618.
doi:10.2514/1.C034696

[13] Loeffler, I. J., "Structureborne Noise Control in Advanced Turboprop Aircraft," NASA TM-88947, Jan. 1987.

[14] van Arnhem, N., Sinnige, T., Stokkermans, T. C. A., Eitelberg, G., and Veldhuis, L. L. M., "Aerodynamic Interaction Effects of Tip-Mounted Propellers Installed on the Horizontal Tailplane," *2018 AIAA Aerospace Sciences Meeting*, AIAA Paper 2018-2052, Jan. 2018.
doi:10.2514/6.2018-2052

[15] Martinez, R., "Predictions of Wing and Pylon Forces Caused by Propeller Installation," NASA CR-178298, May 1987.

[16] Unruh, J. F., "Aircraft Propeller Induced Structure-Borne Noise," NASA CR-4255, Oct. 1989.

[17] Tinetti, A. F., "On the Use of Surface Porosity to Reduce Wake-Stator Interaction Noise," Ph.D. Thesis, College of Engineering, Virginia Polytechnic Inst. and State Univ., Blacksburg, VA, 2001.

[18] Tinetti, A. F., Kelly, J. J., Bauer, S. X. S., and Thomas, R. H., "On the Use of Surface Porosity to Reduce Unsteady Lift," *15th AIAA Computational Fluid Dynamics Conference*, AIAA Paper 2001-2921, June 2001.
doi:10.2514/6.2001-2921

[19] Tinetti, A. F., Kelly, J. J., Thomas, R. H., and Bauer, S. X. S., "Reduction of Wake-Stator Interaction Noise Using Passive Porosity," *40th AIAA Aerospace Sciences Meeting and Exhibit*, AIAA Paper 2002-1036, Jan. 2002.
doi:10.2514/6.2002-1036

[20] Lee, S., "Reduction of Blade-Vortex Interaction Noise Through Porous Leading Edge," *AIAA Journal*, Vol. 32, No. 3, 1994, pp. 480–488.
doi:10.2514/3.12011

[21] Vergara Torralba, C., Bilka, M., and Schram, C., "Experimental and Analytical Study of Tonal Source Attenuation in Wake-Stator Interaction with Porous Material," *14th International Symposium on Transport Phenomena and Dynamics of Rotating Machinery (ISROMAC-14)*, Feb. 2012.

[22] Raghunathan, S., "Passive Control of Shock-Boundary Layer Interaction," *Progress in Aerospace Sciences*, Vol. 25, No. 3, 1988, pp. 271–296.
doi:10.1016/0376-0421(88)90002-4

[23] Roger, M., Schram, C., and De Santana, L., "Reduction of Airfoil Turbulence-Impingement Noise by Means of Leading-Edge Serrations and/or Porous Material," *19th AIAA/CEAS Aeroacoustics Conference*, AIAA Paper 2013-2108, May 2013.
doi:10.2514/6.2013-2108

[24] Angland, D., Zhang, X., and Molin, N., "Measurements of Flow Around a Flap Side Edge with Porous Edge Treatment," *AIAA Journal*, Vol. 47, No. 7, 2009, pp. 1660–1671.
doi:10.2514/1.39311

[25] Bae, Y., and Moon, Y. J., "Effect of Passive Porous Surface on the Trailing-Edge Noise," *Physics of Fluids*, Vol. 23, No. 12, 2011, Paper 126101.
doi:10.1063/1.3662447

[26] Geyer, T., Sarradj, E., and Fritzsche, C., "Measurement of the Noise Generation at the Trailing Edge of Porous Airfoils," *Experiments in Fluids*, Vol. 48, No. 2, 2010, pp. 291–308.
doi:10.1007/s00348-009-0739-x

[27] Abbott, I. H., Von Doenhoff, A. E., and Stivers, L. S., Jr., "Summary of Airfoil Data," NACA TR-824, Jan. 1945.

[28] Scarano, F., and Riethmuller, M. L., "Iterative Multigrid Approach in PIV Image Processing with Discrete Window Offset," *Experiments in Fluids*, Vol. 26, No. 6, 1999, pp. 513–523.
doi:10.1007/s003480050318

[29] Wieneke, B., "PIV Uncertainty Quantification from Correlation Statistics," *Measurement Science and Technology*, Vol. 26, No. 7, 2015, Paper 074002.
doi:10.1088/0957-0233/26/7/074002

[30] van Oudheusden, B. W., "PIV-Based Pressure Measurement," *Measurement Science and Technology*, Vol. 24, No. 3, 2013, Paper 032001.
doi:10.1088/0957-0233/24/3/032001

[31] Ragni, D., van Oudheusden, B. W., and Scarano, F., "3D Pressure Imaging of an Aircraft Propeller Blade-Tip Flow by Phase-Locked

Stereoscopic PIV," *Experiments in Fluids*, Vol. 52, No. 2, 2012, pp. 463–477.
doi:10.1007/s00348-011-1236-6

[32] Ragni, D., Simão Ferreira, C., and Correale, G., "Experimental Investigation of an Optimized Airfoil for Vertical-Axis Wind Turbines," *Wind Energy*, Vol. 18, No. 9, 2015, pp. 1629–1643.
doi:10.1002/we.1780

[33] Brandt, A., "Statistics and Random Processes," *Noise and Vibration Analysis: Signal Analysis and Experimental Procedures*, 2nd ed., Wiley, New York, 2011, pp. 65–71.

[34] Dougherty, R. P., "Beamforming In Acoustic Testing," *Aeroacoustic Measurements*, edited by T. J. Mueller, Springer–Verlag, Berlin, 2002, pp. 62–97.

[35] Sijtsma, P., "Phased Array Beamforming Applied to Wind Tunnel and Flyover Tests," National Aerospace Lab./NLR TP-2010-549, Amsterdam, Dec. 2010.

[36] Arce León, C., Merino-Martínez, R., Ragni, D., Avallone, F., and Snellen, M., "Boundary Layer Characterization and Acoustic Measurements of Flow-Aligned Trailing Edge Serrations," *Experiments in Fluids*, Vol. 57, Dec. 2010, Paper 182.
doi:10.1007/s00348-016-2272-z

[37] Lord Rayleigh, F. R. S., "XXXI. Investigations in Optics with Special Reference to the Spectroscope," *London, Edinburgh, and Dublin Philosophical Magazine and Journal of Science*, Vol. 8, No. 49, 2009, pp. 261–274.
doi:10.1080/14786447908639684

[38] Avallone, F., Casalino, D., and Ragni, D., "Impingement of a Propeller-Slipstream on a Leading Edge with a Flow-Permeable Insert: A Computational Aeroacoustic Study," *International Journal of Aeroacoustics*, Vol. 17, Nos. 6–8, 2018, pp. 687–711.
doi:10.1177/1475472X18788961

[39] Mineck, R. E., and Hartwich, P. M., "Effect of Full-Chord Porosity on Aerodynamic Characteristics of the NACA 0012 Airfoil," NASA TP-3591, April 1996.

[40] Veldhuis, L. L. M., "Propeller Wing Aerodynamic Interference," Ph.D. Thesis, Faculty of Aerospace Engineering, Delft Univ. of Technology, Delft, The Netherlands, 2005.